Taiwan Earth System Model Version 1: Description and Evaluation of Mean State

Wei-Liang Lee[1], Yi-Chi Wang[1], Chein-Jung Shiu[1], I-chun Tsai[1], Chia-Ying Tu[1], Yung-Yao Lan[1], Jen-Ping Chen[2], Hua-Lu Pan[3], and Huang-Hsiung Hsu[1]

[1] Research Center for Environmental Changes

[2] National Taiwan University

[3] National Center for Environmental Protection

Correspondence: Wei-Liang Lee (leelupin@gate.sinica.edu.tw)

Abstract.

The Taiwan Earth System Model (TaiESM) version 1 is developed based on Community Earth System Model version 1.2.2 of National Center for Atmospheric Research. Several innovated physical and chemical parameterizations, including trigger functions for deep convection, cloud macrophysics, aerosol, and three-dimensional radiation–topography interaction, as well as a one-dimensional mixed-layer model optional for the atmosphere component, are incorporated. The precipitation variability, such as diurnal cycle and propagation of convection systems, is improved in TaiESM. TaiESM demonstrates good model stability in the 500-year preindustrial simulation in terms of the net flux at the top of the model, surface temperatures, and sea ice concentration. In the historical simulation, although the warming before 1935 is weak, TaiESM well captures the increasing trend of temperature after 1950. The current climatology of TaiESM during 1979–2005 is evaluated by observational and reanalysis datasets. Cloud amounts are too large in TaiESM, but their cloud forcing is only slightly weaker than observational data. The mean bias of the sea surface temperature is almost zero, whereas the surface air temperatures over land and sea ice regions exhibit cold biases. The overall performance of TaiESM is above average among models in Coupled Model Intercomparison Project phase 5, particularly that the bias of precipitation is smallest. However, several common discrepancies shared by most models still exist, such as the double Intertropical Convergence Zone bias in precipitation and warm bias over the Southern Ocean.

1. Introduction

The Earth system model (ESM) is a state-of-the-art tool that can simulate the long-term evolution of the climate system including the atmosphere, ocean, land, and cryosphere and provide future projections from the scientific aspect to study the impact of global climate change on the natural environment, ecosystem, and human society (IPCC 5th Assessment Report, 2013). Because of the constraint of computing power, the spatial resolution of ESMs participated in the Coupled Model Intercomparison Project Phase 5 (CMIP5; Taylor et al. 2012) is generally on the order of approximately 100 km. However, this coarse resolution is unsuitable for climate studies in the Taiwan area because this island is 400 km long and 150 km wide, which occupies only several grid boxes in these ESMs. For the Taiwanese scientific community, developing a global model to provide climate data in various future scenarios with high temporal resolutions—daily or hourly—for dynamical or statistical downscaling is desirable. Taiwan's National Science Council (now Ministry of Science and Technology) has accordingly launched a project to increase climate modeling capability and capacity in Taiwan, the core component of which is Taiwan Earth System Model (TaiESM) development.

In Taiwan, manpower and expertise for climate research are limited; thus, we could not create an ESM from scratch. Therefore, TaiESM version 1 is developed on the basis of the Community Earth System Model version 1.2.2 (CESM1.2.2; Hurrell et al., 2013) from National Center for Atmospheric Research (NCAR) sponsored by National Science Foundation and the Department of Energy of the United States. TaiESM consists of the Community Atmosphere Model version 5.3 (CAM5), Community Land Model version 4 (CLM4), Parallel Ocean Program version 2 (POP2), and Community Ice Code version 4 (CICE4). We replace or modify existing parameterizations in CAM5, including new trigger functions for the deep convection scheme (Wang et al., 2015b), new cloud macrophysics scheme for cloud fraction calculation (Shiu et al., 2020), and a three-moment aerosol scheme (Chen et al., 2013). A novel parameterization for the impact of three-dimensional (3D) radiation–topography interactions (Lee et al., 2013) is added to CLM4. In addition, a one-dimensional

(1D) mixed-layer ocean model with a high vertical resolution (Tsuang et al., 2009) is used for CAM5 with slab ocean simulation in TaiESM.

An object of TaiESM development is to improve the simulations of climate variability in various spatial and temporal scales for more reliable climate projections in Taiwan. Weather and climate in Taiwan is deeply affected by capricious East Asia/western North Pacific monsoon and typhoons. In addition, because of its small size and steep terrain, predicting the frequencies of severe weather and heavy precipitation in Taiwan is highly difficult (Hsu et al., 2011). Therefore, the parameterizations selected for TaiESM are for enhancing variability simulation. The trigger functions for the deep convection scheme in TaiESM, adopted from National Centers for Environmental Prediction (NCEP) Global Forecast System (GFS) with Simplified Arakawa–Schubert scheme (SAS; Pan and Wu, 1995; Han and Pan, 2011), aim to improve the timing of convective precipitation occurrence. As demonstrated by Lee et al. (2008), by using GFS, these trigger functions are key to improved simulations of the diurnal rainfall cycle over the Southern Great Plains (SGP) in the United States. The parameterization for 3D radiation-topography interactions accounts for the effects of shadows and reflections from subgrid topographic variation on the surface solar flux (Lee et al., 2011) designed for application to general circulation models (GCMs). The high-resolution 1D mixed-layer model can resolve fast change in the skin temperature of the sea surface (Tu and Tsuang, 2005).

The organization of this paper is as follows: Section 2 describes TaiESM, particularly the new and modified schemes different from CESM1.2.2. Section 3 presents the design of model experiments. Sections 4 and 5 provide the description of TaiESM performance in preindustrial and historical simulations, respectively. Summary and conclusions are given in Section 6.

2. Model description

The development of TaiESM is based on CESM1.2.2, in which the ocean, sea ice, and river components, as well as the infrastructure of the model, remain unchanged. For the atmosphere, several

84 physical and chemical parameterizations are modified, as two trigger functions are added to the default
85 deep convection scheme, and cloud macrophysics and aerosol schemes are replaced. A
86 parameterization of surface albedo adjustment is added to CLM4 to account for the topographic effect
87 on surface solar radiation. In addition, a 1D mixed-layer ocean model is integrated to TaiESM for
88 simulations of CAM5 coupled with a slab ocean.
89
90 **2.1. Atmosphere**
91 The atmosphere model in TaiESM is based on CAM version 5.3 (Neale et al., 2010). The dynamic
92 core is finite volume (Lin, 2004) in a hybrid sigma-pressure vertical coordinate. The Rapid Radiative
93 Transfer Model for GCMs (RRTMG; Iacono et al., 2008) with two-stream approximation, correlated
94 *k*-distribution, and Monte Carlo Independence Column Approximation (McICA; Pincus et al., 2003)
95 is employed to calculate radiative fluxes and heating rates in the atmosphere. The shallow convection
96 and moist turbulence schemes are based on those reported by Park and Bretherton (2009) and
97 Bretherton and Park (2009), respectively. A two-moment cloud microphysics scheme (Morrison and
98 Gettelmen, 2008) is used to predict changes in the mass and number of cloud droplets and to diagnose
99 stratiform precipitation.
100
101 **2.1.1. Trigger function for deep convection**
102 Convective trigger function is a critical part of the cumulus parameterization scheme to determine
103 the initiation of precipitating convection and thus has a critical role in rainfall variability simulation.
104 With the Zhang–McFarlane scheme framework (Zhang and McFarlane, 1995; Neale et al., 2008),
105 TaiESM has adopted two convection triggers proposed by Wang et al. (2015b): unrestricted launching
106 level (ULL) and convective inhibition (CIN). By modifying the deep convection scheme in
107 CESM1.0.3/CAM5.1, Wang et al. (2015b) reported significant improvements in the diurnal rainfall
108 peak at the Atmospheric Radiation Measurement (ARM) SGP site, mainly because of the suppression

of daytime spurious convection by the CIN trigger and initiation of nighttime mid-level convection by ULL trigger. ULL may also aid in improving diurnal rainfall phase in many other areas worldwide when implemented in the newly developed Energy Exascale Earth System Model version 1 (E3SMv1) of the U.S. Department of Energy (Xie et al., 2019).

Similar to that in E3SM, improvement in the diurnal rainfall cycle is found in TaiESM. Figure 1 displays local times (LTs) of the diurnal rainfall peak occurrence, referred to as the peak phase from the 11-year (2001–2011) Tropical Rainfall Measuring Mission (TRMM) merged satellite data (Huffman et al. 2007) and the historical model runs during 1979–2005. Areas with amplitude of diurnal rainfall cycle smaller than 0.5 mm day^{-1} are masked to emphasize the regions with strong diurnal rainfall signals. Two distinct changes in diurnal rainfall cycle are found in TaiESM compared with those in CESM1.2.2. First, the simulated diurnal rainfall peak over the tropical lands is improved. For example, the observed peaks in the Central Africa (Box A) and the Amazon basin (Box B) occur around 20-22 LT and 18-20 LT, respectively. These peaks are delayed from 12–14 LT in CESM1.2.2 to 14-18 LT in TaiESM. A similar delay is also found in islands such as Borneo and Sumatra. As a result, nocturnal rainfall in TaiESM is increased compared with that in CESM1.2.2.

Second, the propagation of convective organizations is better simulated. Propagating convective systems originated from coastlines or topographical regions could be demonstrated by the gradual phase change in Figure 1, such as the eastern slope of the Rocky Mountains (Box C) and northern South America (north of Box B). More specifically, Figure 2 shows the Hovmöller diagram of longitude and local time for TaiESM, CESM1.2.2, and TRMM observations over SGP (35°N–40°N, 90°W–110°W) in Box C. Convection occurs at 104°W in the evening and propagates eastward in the observation (Carbone and Tuttle, 2008). In CESM1.2.2, convection occurs in the early afternoon and peaks before midnight, but it is stationary at the same location. TaiESM successfully captures the eastward propagation of the rainfall and a better occurrence time of convection in the late afternoon, as well as the more realistic rainfall intensity. This result is consistent with the single-column model

tests of Wang et al. (2015b), indicating that their proposed convective trigger may be the cause of these improvements. Furthermore, Wang and Hsu (2019) demonstrate that the improvement of nocturnal rainfall over SGP is mainly from the superior response of the ULL + CIN convective trigger to the low-level convergence between the branch of mountain-plain solenoid and low-level jet from Gulf of Mexico. With the horizontal resolution at an order of 100 km, this result suggests that the convective trigger of TaiESM captures the large-scale preconditioning related to the convective organization there (Dirmeyer et al., 2011), rather than only the convective systems itself.

2.1.2. Cloud fraction

The cloud macrophysics scheme used in TaiESM is the GFS–TaiESM–Sundqvist (GTS) scheme (Shiu et al., 2020). Its prototype was first developed for the NCEP GFS model and has been further modified for the TaiESM. Similar to that in many numerical weather prediction and global climate models, the GTS scheme is based on the Sundqvist scheme (Sundqvist et al., 1989), which calculates changes in cloud condensates in a grid box on the basis of the budget equation for relative humidity (RH) with large-scale advection. The CAM5 macrophysics (Park et al., 2014) follows this approach and assumes empirical values of critical RH (RH_c) as the threshold of condensation. The key difference of the GTS scheme from the CAM5 macrophysics is the re-derivation of the equation relating the change in the subgrid-scale cloud condensate using the distribution width of mixing ration of total water (q_t) to replace RH_c, as indicated in Tompkins (2005). The unnecessary use of RH_c is consequently removed to allow an improved correlation among cloud fraction, RH, and condensates.

Figure 3 illustrates cloud fraction as a function of RH of water vapor (q_v/q_s) and RH of condensates (q_l/q_s) for the CAM5 macrophysics and the GTS schemes with uniform and triangular probability density functions (PDFs) of q_t in a grid box. Given the same RH of water vapor, the PDF-based calculation allows larger cloud fraction if more cloud condensates exist in the grid box than the CAM5 macrophysics. The difference in cloud fraction produced by the two PDFs is small, implying that this

159 scheme might not be very sensitive to the shape of the distribution. The triangular PDF provides
160 additionally rapid changes in cloud fraction when the RH of condensates and water vapor changes,
161 and it is used as the default PDF of the GTS scheme.
162
163 **2.1.3. Aerosol**
164 The aerosol parameterization used in TaiESM is the Statistical-Numerical Aerosol
165 Parameterization (SNAP; Chen et al., 2013). SNAP is a bulk parameterization, and the modal approach
166 (Seigneur et al., 1986; Whitby and McMurry, 1997) is adopted to describe the particle size distribution.
167 In contrast to conventional aerosol parameterizations in most ESMs, changes in the zeroth moment
168 (number), second moment (surface area), and third moment (mass) due to physical processes are
169 tracked in SNAP. The physical processes included in SNAP are emission, nucleation, coagulation,
170 condensation, mixing, as well as dry and wet deposition. SNAP has been applied to the US EPA
171 Models-3/Community Multi-scale Air Quality (CMAQ; Byun and Schere, 2006) modeling system and
172 been verified by observations (Chen et al., 2013; Tsai et al., 2015) with Weather Research and
173 Forecasting Model (WRF; Skamarock et al., 2005).
174
175 **2.2. Land**
176 The land model in TaiESM is CLM4 (Oleson et al., 2010; Lawrence et al., 2011). The surface
177 albedo is primarily a function of vegetation, soil moisture, solar zenith angle, as well as snow
178 reflectivity calculated by the Snow, Ice, and Aerosol Radiative Model (SNICAR; Flanner and Zender,
179 2006), which considers the aerosol deposition of black carbon and dust, effective size of snow grains,
180 and vertical profile of heating. As the albedo of a grid box is determined, it is then adjusted to include
181 the topographic effect on surface solar radiation.
182 The parameterization for 3D radiation–topography interactions is to evaluate the impact of
183 topography on surface solar radiation, including insolation on various slopes and aspects, shadow cast

by nearby mountains, and reflections between surfaces (Lee et al., 2013). It is developed on the basis of numerous "exact" Monte Carlo calculation that simulates the scattering, reflection, and absorption of photons within the 3D atmosphere and surface (Chen et al., 2006; Liou et al., 2007; Lee et al., 2011). The parameterization adjusts surface albedo so that the solar radiation absorbed by the surface in the land model corresponds with the results of the Monte Carlo calculation. Several geographic parameters are used for input, including the slope, aspect, sky view factor, terrain configuration factor, standard deviation of elevation within a grid box, and solar zenith and azimuth angles. Gu et al. (2012) and Liou et al. (2013) demonstrate that this topographic effect can increase the amount of snowpack in the valley and enhance the snowmelt in mountains in the WRF simulations over the western United States. Lee et al. (2015, 2019) also demonstrate that incorporating this parameterization to the Community Climate System Model version 4 (CCSM4) can significantly improve the surface energy budget over the Rocky Mountains and the Tibetan Plateau and thus reduce the systematic cold bias in the CMIP5 models.

2.3. Ocean, sea ice, and river

The sea ice and dynamic ocean components of TaiESM are from the CICE4 (Hunke and Lipscomb, 2008) and POP2 (Smith et al., 2010) of Los Alamos National Laboratory, respectively. The River Transport Model (RTM; Oleson et al., 2010) is designed to route liquid and ice runoff to the ocean as one of the freshwater input to POP2. The configurations of CICE4, POP2, and RTM in the fully coupled TaiESM simulations are identical to those in CESM1.2.2. Note that there is no land ice model in TaiESM. Therefore, the formation of sea ice from the discharge of ice sheet to the ocean is not simulated.

To save computational resources, a zero-dimensional slab ocean model without dynamical process is commonly used to simulate the thermodynamic interaction between the atmosphere and ocean. In TaiESM, an efficient 1D mixed-layer model is coupled with the atmosphere component to reveal the impact of the fast evolution in upper ocean layers. The one-column ocean model Snow–Ice–

Thermocline (SIT; Tu and Tsuang, 2005; Tsuang et al. 2009) is designed to simulate the sea surface temperature (SST) and upper ocean temperature variations with a high vertical resolution, including cool skin, diurnal warm layer, and mixed-layer of the upper ocean. SIT calculates changes in temperature, momentum, salinity, and turbulent kinetic energy driven by vertical fluxes parameterized using the classical K approach. Cool skin is derived by considering merely molecular transport for vertical diffusion of heat in the skin layer, where the skin layer thickness is calculated as described by Artale et al. (2002). Beneath the skin layer, eddy diffusivity is determined according to a second-order turbulence closure approach (Gaspar et al., 1990), and the 1-m vertical discretization is deployed down to a 10-m depth for resolving diurnal warm layer. Because of the lack of ocean circulation in the one-column ocean model, the calculated ocean temperatures are weakly nudged to climatology for ocean below 10-m depth to avoid climate drift. SIT and AGCM exchange SST and fluxes at every time step in tropics (30°S–30°N), whereas climatological SST drives the AGCM elsewhere. Note that SIT is not integrated with the dynamic ocean model (POP2); therefore, fully coupled TaiESM simulations do not include SIT.

2.4. Model tuning

The preliminary version of TaiESM was very cold compared with CESM1.2.2 using the preindustrial greenhouse gas concentrations and aerosol emissions. The most apparent change was the significant increase in cloud cover, particularly low clouds, which was probably induced by GTS cloud macrophysics and SNAP aerosol schemes. Therefore, several parameters associated with cloud formation were adjusted to reduce shortwave cloud forcing. We first explored that aerosol-cloud interactions were very strong in TaiESM with SNAP scheme. Therefore, the activation rate of aerosols to cloud condensation nuclei was reduced by 10% in the microphysics scheme to weaken the aerosol indirect effect. The sizes of detrained liquid particles from shallow convection and solid particles from deep convection were increased from 10 μm in CESM1.2.2 to 14 μm and from 15 to 25 μm,

234 respectively. Larger detrained particles have smaller cloud optical depth and shorter suspension time
235 in the air when the detrained water content is the same. Both effects can reduce cloud albedo. Although
236 RH_c is removed from GTS scheme for grid boxes with the presence of condensates, it is still required
237 for the formation of clouds in a cloud-free grid box. The value of RH_c was increased from 0.8 in the
238 free atmosphere in CESM1.2.2 to 0.85 in TaiESM to make cloud formation less efficient. After these
239 adjustments, the global mean surface temperature of TaiESM in the preindustrial simulation is
240 comparable to that of CESM1.2.2 while the radiation imbalance at the top of the atmosphere (TOA) is
241 minimized. Note that this model tuning is made only at the spatial resolution of about 1°. Additional
242 tuning would be required for stable simulations at higher or lower resolutions.
243
244 **3. Experiment design**
245 The horizontal resolution of the atmosphere and land in TaiESM is 0.9° latitude by 1.25° longitude,
246 with 30 vertical layers and a model top at 2 hPa in the atmosphere. The ocean and sea ice components
247 use the same horizontal resolution with 320 × 384 grid points (approximately 1°) and 60 vertical layers
248 in the ocean. TaiESM is spun-up using CMIP5 preindustrial conditions, such as greenhouse gas
249 concentrations, surface aerosol emissions, solar constant, and land-use types. Because TaiESM is
250 considerably similar to CESM1.2.2, we use the model restart files of CESM1.2.2 for the 1850 control
251 run as the initial condition to reduce the computational effort, particularly for the ocean component
252 that may need more than a thousand years to reach a steady state. The spin-up integration continues
253 for 500 years, and the climate state at the end of year 500 is used as the initial condition for the 500-
254 year preindustrial control (hereafter piControl) simulation. The historical simulation then starts at the
255 end of piControl (i.e., year 1000) with observationally based forcing, including changes in the solar
256 constant, greenhouse gas concentrations, surface aerosol emission, and volcanic eruptions, from 1850
257 to 2005.
258

4. Model stability in piControl run

In this section, the global means of several climatological variables in piControl run of TaiESM are evaluated. The climate drift from CESM1.2.2 initial conditions to TaiESM equilibrium during the spin-up is also assessed to represent differences between the two models caused by the new or modified physical processes in TaiESM.

4.1. Time series of climate states

Figure 4 illustrates the time series of several global mean variables in TaiESM piControl. The long-term global mean TOA net flux is 0.086 W m^{-2}, and it decreases by 0.0054 W m^{-2} in 500 years but insignificantly. Furthermore, the mean surface net flux is 0.081 W m^{-2} with an almost identical decreasing trend as TOA net flux. The imbalance at TOA causes heating of the whole model system, and the comparatively less imbalance at the surface indicates a smaller part of excessive energy remains in the atmosphere in piControl. Consequently, the long-term trend of surface air temperature (SAT) is 0.0088 K $century^{-1}$ in 500 years, which is statistically significant. By contrast, the trend of SST is 0.0047 K $century^{-1}$, only about half of the SAT trend and insignificant. By breaking down the surface net flux, we found that the energy exchange between the atmosphere and land is less than 10^{-5} W m^{-2}, whereas the net flux into the ocean is 0.114 W m^{-2} (figures not shown). The excessive energy enters the deep ocean and leads to a steady increase in global mean ocean temperature of 0.030 K $century^{-1}$. Therefore, even after a 1000 years' simulation, the system does not reach the thermodynamic equilibrium. In addition, considering that the heat capacity of the entire ocean is approximately 1000 times larger than the atmosphere, the heating rates of the atmosphere caused by the residual net flux (0.005 W m^{-2}) is too small compared with the heating rate of the ocean. It implies that an unknown energy leak may exist in the coupling between the atmosphere and ocean, which requires further investigation in programming to fix this problem.

The annual mean time series of sea ice area in the Northern Hemisphere (NH) and Southern

284 Hemisphere (SH) are exhibited in the bottom panels of Figure 4. The Arctic sea ice has a small but
285 significant trend of -0.01×10^6 km^2 century^{-1}, corresponding to the slight warming of the entire model
286 fairly well. By contrast, the linear trend of the sea ice area in the Southern Ocean over the 500-year
287 span is almost zero, even though the variation is much larger. The minimal change in the sea ice area
288 indicates that the energy gain of the cryosphere could be negligible compared with other model
289 components. The global mean sea surface salinity (SSS) reduces significantly by -0.0036 g kg^{-1}
290 century^{-1}. However, it can be found that SSS is almost constant with a slope of about 10^{-4} g kg^{-1}
291 century^{-1} after year 700. On the other hand, there is a small but significant decreasing trend of the
292 global mean ocean salinity of 1.3×10^{-4} g kg^{-1} century^{-1}, which is very close to the trend of SSS in
293 the last 300 years.
294
295 **4.2. Comparison with CESM**
296 The long-term means of several variables in piControl runs performed by CESM1.2.2 and TaiESM
297 are listed in Table 1. The TOA net flux in TaiESM and CESM1.2.2 are both within 0.09 W m^{-2}. The
298 magnitude of imbalance is acceptable, but it could lead to warming of the entire Earth system. The
299 SAT and SST in TaiESM are higher than those in CESM1.2.2 by 0.42 and 0.23 K, respectively.
300 Shortwave (SW) net flux at TOA in TaiESM is larger than CESM1.2.2 by 2.24 W m^{-2}, which might
301 be the primary cause of higher surface temperatures and consequently result in larger longwave (LW)
302 net flux at TOA of 2.23 W m^{-2}. The difference in the clear-sky net SW flux at TOA is only 0.66 W
303 m^{-2}, suggesting that the surface albedo difference is small, whereas the contribution from the
304 difference in cloud reflection is larger. Although the high and low cloud covers in TaiESM are larger
305 than those in CESM1.2.2, the magnitude of SW cloud forcing (SWCF) is smaller in TaiESM. It
306 indicates that clouds in TaiESM are less reflective than that those in CESM1.2.2. By contrast, the
307 differences in clear-sky net LW flux at TOA and LW cloud forcing (LWCF) are 1.67 and 0.59 W m^{-2},
308 respectively; therefore, the warmer surface and atmosphere have greater contribution to additional

outgoing longwave radiation (OLR) in TaiESM. However, the amount of high cloud in TaiESM is substantially larger than that in CESM1.2.2. This implies that the high clouds in TaiESM could be optically thinner. The different relation between cloud forcing and cloud cover in SW and LW in TaiESM is probably be due to the GTS scheme, which can produce larger fraction but less dense clouds compared with the cloud macrophysics scheme in CAM5.

5. Historical simulation

In this section, we evaluate the performance of TaiESM historical simulation against the observation or reanalysis data. The temporal evolution of global mean temperature from the preindustrial to present day is assessed. The mean states of the current climate, defined as the period of 1979–2005, in the historical simulation are used for comparison. The behavior of El-Niño–Southern Oscillation (ENSO) in TaiESM is also evaluated.

5.1. Global mean temperature evolution

Figure 5 illustrates changes in global mean near-surface temperature anomaly of TaiESM and two observations, Berkeley Earth Surface Temperature (BEST; Rohde et al., 2013) and Goddard Institute for Space Studies Surface Temperature (GISTEMP; Lenssen et al., 2019), by using the mean temperature of 1951–1980 as the benchmark. The warming trend of TaiESM is weaker than the observation data during 1850–1935. The evolution of SAT in TaiESM exhibits fluctuation similar to observations, particularly before 1900, but with smaller amplitudes. The magnitudes of cooling induced by major volcanic eruptions, such as Krakatoa (1883), Santa Maria (1902), Agung (1963), and Pinatubo (1991), in TaiESM is close to those in the observational data, implying that the radiative forcing due to stratospheric aerosols is in good agreement with the observations. After 1950, the change in SAT of TaiESM follows the observations and captures the trend of global warming very well. The warming rate of TaiESM during 1950–2005 is 1.12 K century^{-1}, comparable with 1.16 and

334 1.27 K century^{-1} of BEST and GISTEMP, respectively.

335

336 **5.2. Cloud and radiation**

337 Figure 6a demonstrates the comparison in the total cloud fraction between TaiESM and Moderate
338 Resolution Imaging Spectroradiometer (MODIS) Level 3 product during 2001–2012. TaiESM
339 overestimates the total cloud fraction by approximately 3% globally with a root mean square difference
340 (RMSD) of 14.07. Almost all of the Arctic Ocean is overcast in TaiESM, which is approximately 30%
341 higher than observational data. Cloud fraction is also severely overestimated over the Antarctic
342 continent and the Southern Ocean. TaiESM produces too much cloud over the southern branch of the
343 Intertropical Convergence Zone (ITCZ) in the central and eastern Pacific, implying the prevalence of
344 double ITCZ, which will be discussed in a subsequent section. Excessive amount of clouds is also
345 noted in the maritime continent, western equatorial Indian Ocean, and most of the land areas. By
346 contrast, cloud fraction is remarkably underestimated in the Amazon basin and the subtropical ocean,
347 particularly the stratocumulus near the western coasts of continents. Compared with the synergic
348 CloudSat and Cloud-Aerosol Lidar with Orthogonal Polarization (CALIOP) data during 2006–2010
349 (Kay and Gettelman, 2009), low clouds in TaiESM are systematically underestimated over the entire
350 tropical and subtropical regions, as shown in Figure 6c, whereas they are overestimated in high-latitude
351 areas. The total cloud fraction in the tropics is high because of excessive high cloud in the model
352 (Figure 6b).

353 Clouds can substantially modulate the radiation field because of its high reflectivity in SW and
354 high absorptivity in LW. Figure 7a illustrates the comparison of SWCF in TaiESM with that in Clouds
355 and the Earth's Radiant Energy System–Energy Balanced and Filled data (CERES–EBAF; Kato et al.,
356 2018) over 2000–2015. In terms of the global mean, SWCF in TaiESM is very close to that of the
357 observational data by 0.19 W m^{-2} larger. Although there is excessive cloud over the polar regions,
358 such as the Southern Ocean near the Antarctic continent and almost all of the Arctic Ocean, in TaiESM,

SWCF is not as strong as that in the observational data. It could be contributed from the optically thin polar clouds due to GTS cloud macrophysics scheme and from the positive bias of sea ice albedo in the Arctic Ocean in TaiESM (not shown). In the subtropical and tropical regions, SWCF generally follows the spatial pattern of total cloud fraction that a larger cloud fraction produces stronger SWCF, such as the storm track in the North Pacific, southern branch of ITCZ, maritime continent, western tropical Indian Ocean, and south of the Sahara Desert. However, SWCF is too strong over the Amazon basin in TaiESM, even though there is underestimated amount of clouds. By contrast, because of underestimated total cloud fraction, SWCF in TaiESM is too weak over the stratocumulus areas off the California and Peru coasts as well as over the subtropical Pacific, Atlantic, and Indian Oceans in the SH.

The global mean of LWCF in TaiESM is significantly weaker than that in CERES–EBAF by 4.31 W m^{-2}. As illustrated in Figure 7b, TaiESM underestimates LWCF worldwide, and the magnitude of LWCF bias generally follows the bias of high cloud. Positive LWCF bias only exists in some regions over the tropical ocean with too many high clouds in TaiESM. However, although more high clouds exist along the northern branch of ITCZ, LWCF is weaker in the model. The remarkable negative LWCF bias seems incompatible with the overestimated high clouds because more high clouds should be able to intercept more LW radiation from the surface. This inconsistency is probably due to the lower altitude of the high clouds or the less dense clouds in TaiESM.

5.3. Surface temperature

Figure 8a illustrates the comparison of SST between TaiESM and Hadley Centre Sea Ice and Sea Surface Temperature dataset (HadISST; Rayner et al., 2003). The regions with a long-term mean sea ice concentration larger than 15% are not used for calculations of the mean and RMSD. The global mean bias of SST in TaiESM is 0.01 K with an RMSD of 1.05 K. The overestimated SST over the Southern Ocean and subtropical South Pacific is probably induced by additional downward SW

384 radiation because of the inaccurate microphysical properties of polar clouds (Kay et al., 2016) and the
385 negative bias of cloud fraction as shown in Figure 6a. The warm bias in the major upwelling regions
386 off the western coasts of Americas and Africa is a common deficiency in many climate models
387 (Griffies et al., 2009), caused by insufficient spatial resolution of the atmosphere and ocean. Warm
388 bias can also be found in North Atlantic including the coast of North America, Labrador Sea, and south
389 of Greenland. Negative biases exist in most of the North Pacific and subtropical North Atlantic,
390 probably because of overestimated wind stress in these regions.

391 Although the SST bias in TaiESM is very small, the global mean SAT in TaiESM is substantially
392 colder than the observational data by 0.49 K with an RMSD of 1.68 K. This result indicates that the
393 temperature over land and sea ice in TaiESM is severely underestimated (Figure 8b). Cold bias exists
394 over most of the polar regions, the Tibetan Plateau, and tropical land areas (e.g., Amazonia, Central
395 Africa, and Southeast Asia). It must be due to the excessive cloud that reflects excessive sunlight. SAT
396 bias over the ocean generally follows SST bias, except that the SAT bias in the subtropical South
397 Pacific is very small despite the warm SST bias.

398

399 **5.4. Precipitation**

400 Figure 9 illustrates the mean precipitation over 1979–2005 in TaiESM and Global Precipitation
401 Climatology Project (GPCP; Huffman et al., 2009) 1-Degree Daily (1-DD) data. TaiESM
402 overestimates the global precipitation by 0.38 mm day^{-1} with an RMSD of 1.11 mm day^{-1}. The most
403 pronounced bias in TaiESM is the double ITCZ—a common issue in most contemporary GCMs (Lin,
404 2007, Hirota and Takayabu, 2013) and in CESM1 (Wang et al., 2015a). The precipitation rates of both
405 the northern and southern ITCZ branches are extremely strong. The overly intense convection
406 strengthens the subsidence and consequently produces too little rainfall along the equator. Precipitation
407 is also overestimated in the maritime continent, while it is severely underestimated in Borneo. In
408 TaiESM, the land–sea contrast in precipitation is not as apparent as in the observation over the warm

409 pool region. The South Pacific convergence zone (SPCZ) is also too strong and too parallel to the
410 ITCZ. The dipole bias in the tropical Indian Ocean, excessive rainfall in the western part and scant
411 rainfall in the eastern part, still exists as in NCAR models (Gent et al., 2011). There is also a double
412 ITCZ bias in the Atlantic Ocean that the southern branch is too strong and the northern branch is too
413 weak. In South America, precipitation over the Amazon basin is considerably underestimated, whereas
414 excessive orographic precipitation can be found along the Andes (Cook et al., 2012).
415
416 **5.5. Sea ice**
417 Figure 10 presents the annual mean of sea ice concentration in the Arctic Ocean and Southern
418 Ocean in TaiESM, and the black lines indicate the 15% mean concentration from the National Snow
419 and Ice Data Center (NSIDC) Climate Data Record (CDR) of passive microwave sea ice concentration
420 version 3 (Peng et al., 2013), during 1979–2005. In the NH, TaiESM severely overestimates sea ice
421 concentration over the North Pacific, particularly in the Sea of Okhotsk. TaiESM also overestimates
422 sea ice in the Barents Sea and near the east coast of Greenland but slightly underestimates sea ice in
423 Labrador Sea. In the SH, sea ice in TaiESM is generally in agreement with the observation. Excessive
424 sea ice is noted in the area south of New Zealand, but in the Indian Ocean region, sea ice is scant. This
425 deviation follows the SST bias presented previously.
426 Figure 11 illustrates the temporal evolution of the annual sea ice concentration in TaiESM
427 compared with that in the CDR. The change in NH sea ice in TaiESM generally captures the trend in
428 the observation before 2002. However, there is an increase in TaiESM in the last 4 years, in contrast
429 to an accelerated reduction in observational data. This sea ice increase could be a fluctuation in a
430 climate simulation, and it requires longer integration for additional investigation. In SH, a decreasing
431 trend of the sea ice concentration can be found in TaiESM, whereas it remains almost unchanged in
432 observational data. Because there is no land ice model in TaiESM, the discharge of the ice sheet from
433 Antarctic continent to Southern Ocean, the major source of SH sea ice, cannot be simulated accurately.

434 Consequently, the sea ice concentration in the SH could be controlled primarily by temperature in
435 TaiESM, leading to an unrealistic temporal evolution.
436
437 **5.6. ENSO**
438 To evaluate the ENSO behavior during 1976-2005 in TaiESM, the HadISST sea surface
439 temperature and MRE2 reanalysis data in the same period are used. The observed and simulated spectra
440 of Nino 3.4 index presented in Figure 12 reveals the adequate ability of TaiESM in reproducing the
441 periodicity of El Niño. The observed Nino 3.4 index exhibits three statistically significant peaks
442 between 2–6 years. TaiESM is able to simulate three spectral peaks with slightly shorter periods, while
443 the amplitudes of all three peaks are larger than observation.
444 The anomalies of surface temperature, sea level pressure, and near-surface wind in December-
445 February when the ENSO is at the mature stage are shown in Figure 13, which are the composites of
446 five and six El Niño events in observation and TaiESM simulation, respectively. The simulated SST
447 anomaly (SSTA) is evidently larger in both amplitude and spatial coverage than the observed and with
448 the maximum shifted westward to the central equatorial Pacific compared with the observation, which
449 is the common bias in many climate models. The horseshoe-like negative SSTA in the
450 northwest/southwest and west of the positive SSTA is stronger and covers much larger areas than the
451 observed one. This over-simulated SSTA structure leads to some marked biases in the simulated
452 atmospheric circulation and temperature, such as the cold bias in the western North Pacific and
453 maritime continent, warm bias in the western Indian Ocean and Bering Sea, and too strong
454 convergence in the eastern equatorial Pacific.
455
456 **5.6. Comparison with CMIP5 models**
457 The overall performance of TaiESM historical simulation during 1979-2005 is evaluated by
458 comparing with other CMIP5 models following the metrics introduced by Gleckler et al. (2008). Figure

14 shows the normalized space-time root-mean-square-error (RMSE) of selected variables from TaiESM, several CMIP5 models, and multi-model ensemble (MME) against reanalysis and observation datasets. The reference data of air temperatures (TA), zonal and meridional wind velocities (UA and VA), and geopotential height (ZG) at various pressure levels, as well as the surface air temperature (TAS), are from Collaborative Reanalysis Technical Environment (CREATE) Multi-Reanalysis Ensemble version 2 (MRE2; Potter et al., 2018). The observational precipitation (PR) data is from GPCP. Upward longwave radiation in the total sky (RLUT) and clear sky (RLUTCS) and upward shortwave radiation in the total sky (RSUT) and clear sky (RSUTCS) are from CERES-EBAF. It is expected that the errors of CMIP5 MME are generally the smallest. TaiESM has smallest bias in PR among all CMIP5 models, and its performance in RSUT and RLUT is also very good. The relative poor performance in TAS is primarily due to the cold bias over land and sea ice areas. The RMSEs of all variables in TaiESM are smaller than the median CMIP5 error, indicating that the performance of TaiESM is above average among all CMIP5 models. The performance of TaiESM is comparable to that of CESM1-CAM5, and they have similar strengths and weaknesses. Note that three variables with RMSE larger than median in CESM1-CAM5 are all improved in TaiESM.

6. Summary and conclusions

This paper documents the TaiESM version 1, developed on the basis of CESM1.2.2, with revised physical and chemical parameterizations, including 1) trigger functions for deep convection, which can improve the variability simulation in convective rainfall; 2) GTS cloud macrophysics scheme to avoid artificial RH threshold for cloud formation; 3) three-moment SNAP aerosol scheme; 4) 3D radiation–topography interactions to account for the impact of shading and reflection on shortwave radiation in mountains. A 1D mixed-layer ocean model is incorporated to the atmosphere component to simulate the thermodynamic air-sea interaction, but it is not used for fully coupled simulations.

TaiESM stability is assessed using 500-year piControl. Although constant imbalance in the net

flux at the TOA exists, the drifts of global mean SAT and SST are very small, with long-term trends of 0.0088 and 0.0047 K century^{-1}, respectively. The excessive energy enters the deep ocean and leads to continuous warming by 0.030 K century^{-1}. The drifts in the sea ice concentration in both NH and SH are both small because of the nearly zero net energy flux from the atmosphere to sea ice. However, the global mean SSS and total ocean salinity both demonstrate significantly decreasing trends.

For the historical evolution of SAT, the warming of TaiESM from 1850 to 1935 is too weak compared with the observation. After 1950, TaiESM satisfactorily captures the trend of global warming with a heating rate of 1.12 K century^{-1} comparable to the observation of 1.16 K century^{-1}.

The current climatology of TaiESM during 1979–2005 is generally in agreement with the observations. The overall performance of TaiESM is better than the median of CMIP5 models, particularly that the RMSE of precipitation is smallest. There are too many clouds in TaiESM, whereas the SWCF and LWCF are mostly similar to and weaker than the observation, respectively. This result implies that the new cloud macrophysics scheme produces larger amount but optically thinner clouds. SST in TaiESM is very close to the observation, whereas SAT is significantly colder, implying remarkably underestimated SAT over land and sea ice surfaces. TaiESM produces excessive precipitation, and the biases of double ITCZ and dipole in the tropical Indian Ocean exist, whereas there is a severe dry bias in the Amazon basin. The trend of the NH sea ice concentration in TaiESM follows the observation well, whereas it might not capture the accelerating reduction in the 21st century. For the ENSO simulation, TaiESM is able to reproduce three spectral peaks similar to observation with periods between 2-6 years while the variability of SST, including magnitude of anomaly and spatial coverage, is too strong.

This paper focuses on the evaluation of long-term climatological state and evolution of global mean quantities in TaiESM in preindustrial and historical simulations. The other part of the characteristics of an ESM, climate variability, is also very critical to the performance of a model, and it requires additional in-depth research. Further investigation of climate variability in TaiESM,

including the intraseasonal oscillation, monsoon, and extreme precipitation, will be documented in the follow-up papers.

Code and data availability. The model code of TaiESM version 1 is available at https://doi.org/10.5281/zenodo.3626654. Output data of TaiESM using CMIP5 forcing, including preindustrial and historical simulations, are available at http://cclics.rcec.sinica.edu.tw/index.php/databases/data.html.

Author contributions. HHH is the initiator and the primary investigator of the TaiESM project. WLL is the main model developer and writes the majority part of the paper. YCW is the developer and writer of trigger functions for deep convection. CJS and YCW are the developer and writers of cloud macrophysics. ICT and JPC are the developers and writers of SNAP aerosol scheme. CYT and YYL are developers of 1D mixed-layer model and CYT is the writer of this section. HLP helps develop the theoretical basis of trigger functions for deep convection and cloud macrophysics.

Competing interests. The authors declare that they have no conflict of interest.

Acknowledgements. The contribution from WLL, YCW, CJS, ICT, CYT, YYL, and HHH to this study is supported by Ministry of Science and Technology of Taiwan under contracts MOST 106-2111-M-001-002, MOST 106-2111-M-034-002, and MOST 106-2111-M-001-005. JPC is also supported by MOST 107-2111-M-001-012. We thank the computational support from National Center for High-performance Computing of Taiwan. This manuscript is edited by Wallace Academic Editing.

References

Artale, V., Iudicone, D., Santoleri, R., Rupolo, V., Marullo, S., and D'Ortenzio, F.: Role of surface

fluxes in ocean general circulation models using satellite sea surface temperature: Validation of and sensitivity to the forcing frequency of the Mediterranean thermohaline circulation, J. Geophys. Res.: Oceans, 107 (C8), 29-1-29-24, 2002.

Bretherton, C. S., and Park, S.: A new moist turbulence parameterization in the Community Atmosphere Model, J. Climate, 22(12), 3422-2448, https://doi.org/10.1175/2008JCLI2556.1, 2009.

Byun, D., and Schere, K. L.: Review of the Governing Equations, Computational Algorithms, and Other Components of the Models-3 Community Multiscale Air Quality (CMAQ) Modeling System, Appl. Mech. Rev., 59(2), 51-77, 2006.

Carbone, R. E., and J. D. Tuttle: Rainfall occurrence in the U.S. warm season: The diurnal cycle, J. Climate, 21(16), 4132–4146, https://doi.org/10.1175/2008JCLI2275.1, 2008.

Chen, J.-P., Tsai, I.-C., and Lin, Y.-C.: A statistical–numerical aerosol parameterization scheme, Atmos. Chem. Phys., 13, 10483-10504, https://doi.org/10.5194/acp-13-10483-2013, 2013.

Chen, Y., Hall, A., & Liou, K. N.: Application of 3D solar radiative transfer to mountains. Journal of Geophysical Research, 111, D21111, https://doi.org/10.1029/2006JD007163, 2006.

Cook, K. H., Meel, G. A., and Arblaster, J. M.: Monsoon regimes and processes in CCSM4, part II: African and American monsoon systems, J. Climate, 25, 2609-2621, https://doi.org/10.1175/JCLI-D-11-00185.1, 2012.

Dirmeyer, P. A., Cash, B. A., Kinter, J. L., Jung, T., Marx, L., Satoh, M., Stan, C., Tomita, H., Towers, P., Wedi, N., Achuthavarier, D., Adams, J. M., Altshuler, E. L., Huang, B., Jin, E. K., and Manganello, J.: Simulating the diurnal cycle of rainfall in global climate models: resolution versus parameterization, Climate Dynamics, 39(1-2), 399–418, https://doi.org/10.1007/s00382-011-1127-9, 2011.

Flanner, M. G. and Zender, C. S.: Linking snowpack microphysics and albedo evolution, J. Geophys. Res., 111, D12208, https://doi.org/10.1029/2005JD006834, 2006.

559 Gaspar, P., Gregoris, Y., and Lefevre, J.-M.: A simple eddy kinetic energy model for simulations of
560 the oceanic vertical mixing: Tests at station Papa and long-term upper ocean study site, J. Geophys.
561 Res. Oceans, 95 (C9), 16179-16193, 1990.
562 Gent, P. R., Danabasoglu, G., Donner, L. J., Holland, M. M., Hunke, E. C., Jayne, S. R., Lawrence, D.
563 M., Neale, R. B., Rasch, P. J., Vertenstein, M., Worley, P. H., Yang, Z.-L., & Zhang, M.: The
564 Community Climate System Model, version 4, J. Climate, 24, 4973–4991, 2011.
565 Gu, Y., Liou, K. N., Lee, W.-L., & Leung, L. R.: Simulating 3-D radiative transfer effects over the
566 Sierra Nevada Mountains using WRF. Atmospheric Chemistry and Physics, 12, 9965–9976,
567 https://doi.org/10.5194/acp-12-9965-2012, 2012.
568 Gleckler, P. J., Taylor, K. E., and Doutriaux, C.: Performance metrics for climate models, J. Geophys.
569 Res., 113, D06104, https://doi.org/10.1029/2007JD008972, 2008.
570 Griffies, S. M., Winton, M., Donner, L. J., horowitz, L. W., Downes, S. M., Farneti, R., Gnanadesikan,
571 A., Hurlin, W. J., Lee, H. C., Liang, Z., Palter, J. B., Samuels, B. L., Wittenberg, A. T., Wyman,
572 B. L., Yin J., and Zadeh, N.: The GFDL CM3 coupled climate model: characteristics of the ocean
573 and sea ice simulations, J. Climate, 24, 3520-3544, https://doi.org/10.1175/2011JCLI3964.1, 2009.
574 Han, J., and Pan, H.-L.: Revision of convection and vertical diffusion schemes in the NCEP global
575 forecast system, Weather and Forecasting, 26(4), 520-533, https://doi.org/10.1175/WAF-D-10-
576 05038.1, 2011.
577 Hirota, N., and Takayabu, Y. N.: Reproducibility of precipitation distribution over the tropical oceans
578 in CMIP5 multi-climate models compared to CMIP3, Climate Dyn., 41, 2909-2920,
579 https://doi.org/10.1007/s00382-013-1839-0, 2013.
580 Hsu, H.-H., Chou, C., Wu, Y.-C., Lu, M.-M., Chen, C.-T., and Chen, Y.-M.: Climate change in Taiwan:
581 Scientific Report 2011 (Summary), National Science Council, Taipei, Taiwan, 67 pp, 2011.
582 Huang, B., Thorne, P. W., Banzon, V. F., Boyer, T., Chepurin, G., Lawrimore, J. H., Menne, M. J.,
583 Smith, T. M., Vose, R. S., and Zhang, H.-M.: Extended reconstructed sea surface temperature,

584 version 5 (ERSSTv5): upgrades, validations, and intercomparisons, J. Climate, 30(20), 8179-8205,
585 https://doi.org/10.1175/JCLI-D-16-0836.1, 2017.
586 Huffman G. J., Adler, R. F., Bolvin, D. T., and Gu, G.: Improving the global precipitation record:
587 GPCP version 2.1, Geophys. Res. Lett., 36, L17808, https://doi.org/10.1029/2009GL040000,
588 2009.
589 Huffman, G. J., Bolvin, D. T., Nelkin, E. J., Wolff, D. B., Adler, R. F., Gu, G., Hong, Y., Bowman, K.
590 P., and Stocker, E. F.: The TRMM multisatellite precipitation analysis (TMPA): quasi-global,
591 multiyear, combined-sensor precipitation estimates at fine scales. J. Hydrometeorol., 8(1), 38–55,
592 https://doi.org/10.1175/JHM560.1, 2007.
593 Hunke, E. C., and Lipscomb, W. H.: CICE: The Los Alamos sea ice model. Documentation and
594 Software User's Manual, Version 4.0, T-3 Fluid Dynamics Group, Los Alamos National
595 Laboratory, Tech. Rep. LA-CC-06-012, 76 pp., 2008.
596 Hurrell, J. W., Holland, M. M., Gent, P. R., Ghan, S., Kay, J. E., Kushner, P. J., Lamarque, J.-F., Large,
597 W. G., Lawrence, D., Lindsay, K., Lipscomb, W. H., Long, M. C., Mahowald, N., Marsh, D. R.,
598 Neale, R. B., Rasch, P., Vavrus, S., Vertenstein, M., Bader, D., Collins, W. D., Hack, J. J., Kiehl,
599 J., and Marshall, S.: The community Earth system model: A framework for collaborative research,
600 B. Am. Meteorol. Soc., 94, 1319–1360, https://doi.org/10.1175/BAMS-D-12-00121, 2013.
601 Iacono, M. J., Delamere, J. S., Mlawer, E. J., Shephard, M. W., Clough, S. A., and Collins, W. D.:
602 Radiative forcing by long-lived greenhouse gases: Calculations with the AER radiative transfer
603 models. J. Geophys. Res., 113, D13103, https://doi.org/10.1029/2008JD009944, 2008.
604 IPCC, Climate Change 2013: The Physical Science Basis. Contribution of Working Group I to the
605 Fifth Assessment Report of the Intergovernmental Panel on Climate Change. Stocker, T. F., Qin,
606 D., Plattner, G.-K., Tignor, M., Allen, S. K., Boschung, J., Nauels, A., Xia, Y., Bex, V., and
607 Midgley, P. M. (eds.). Cambridge University Press, Cambridge, United Kingdom and New York,
608 NY, USA, 1535 pp. 2013.

609 Kato, S., Rose, F. G., Rutan, D. A., Thorsen, T. J., Loeb, N. G., Doelling, et al.: Surface irradiances of
610 Edition 4.0 Clouds and the Earth's Radiant Energy System (CERES) Energy Balanced and Filled
611 (EBAF) Data Product. J. Climate, 31, 4501–4527. https://doi.org/10.1175/JCLI-D-17-0523.1,
612 2018.
613 Kay, J. E., and Gettelman, A.: Cloud influence on and response to seasonal Arctic sea ice loss, J.
614 Geophys. Res., 114, D18, https://doi.org/10.1029/2009JD011773, 2009.
615 Kay, J. E., Bourdages, L., Miller, N. B., Morrison, A., Yettella, V., Chepfer, H., and Eaton, B.:
616 Evaluating and improving cloud phase in the Community Atmosphere Model version 5 using
617 spaceborne lidar observations, J. Geophys. Res. Atmos., 121, 4162-4176,
618 https://doi.org/10.1002/2015JD024699, 2016.
619 Lawrance, D. M., Oleson, K. W., Flanner, M. G., Thornton, P. E., Swenson, S. C., Lawrence, P. J.,
620 Zeng, X., Yang, Z.-L., Levis, S., Sakaguchi, K., Bonan, G. B., and Slater, A. G.: Parameterization
621 improvements and functional and structural advances in version 4 of the Community Land Model,
622 J. Adv. Model. Earth Syst., 3, M03001, https://doi.org/10.1029/2011MS000045, 2011.
623 Lee, W.-L., Liou, K. N., & Hall, A.: Parameterization of solar fluxes over mountain surfaces for
624 application to climate models, Journal of Geophysical Research, 116, D01101,
625 https://doi.org10.1029/2010JD014722, 2011.
626 Lee, W.-L., Liou, K. N., & Wang, C.-c.: Impact of 3-D topography on surface radiation budget over
627 the Tibetan Plateau. Theoretical and Applied Climatology, 113, 95–103,
628 https://doi.org/10.1007/s00704-012-0767-y, 2013.
629 Lee, W.-L., Gu, Y., Liou, K. N., Leung, L. R., & Hsu, H.-H.: A global model simulation for 3-D
630 radiative transfer impact on surface hydrology over Sierra Nevada and Rocky Mountains.
631 Atmospheric Chemistry and Physics, 15, 5405–5413, https://doi.org/10.5194/acp-15-5405-2015,
632 2015.
633 Lee, W.-L., Liou, K.-N., Wang, C.-c, Gu, Y., Hsu, H.-H., and Li, J.-L. F.: Impact of 3-D radiation-

topography interactions on surface temperature and energy budget over the Tibetan Plateau in winter, J. Geophys. Res. Atmos., 124, https://doi.org/10.1029/2018JD029592, 2019.

Lenssen, N., Schmidt, G., Hansen, J., Menne, M., Persin, A., Ruedy, R., and Zyss, D.: Improvements in the GISTEMP uncertainty model, J. Geophys. Res. Atmos., 124, 6307-6326, https://doi.org/10.1029/2018JD029522, 2019.

Lin, S. J.: A "vertically Lagrangian" finite-volume dynamical core for global models. Mon. Wea. Rev., 132, 2293-2307, 2004.

Lin, J.-L.: The double-ITCZ problem in IPCC AR4 coupled GCMs: ocean-atmosphere feedback analysis, J. Climate, 20, 4497-4525, https://doi.org/10.1175/JCLI4272.1, 2007.

Liou, K. N., Lee, W.-L., & Hall, A.: Radiative transfer in mountains: Application to the Tibetan Plateau. Geophysical Research Letters, 34, L23809, https://doi.org/10.1029/2007GL031762, 2007.

Liou, K. N., Gu, Y., Leung, L. R., Lee, W.-L., & Fovell, R. G.: A WRF simulation of the impact of 3-D radiative transfer on surface hydrology over the Rocky Mountains and Sierra Nevada. Atmospheric Chemistry and Physics, 13, 11709–11721, https://doi.org/10.5194/acp-13-11709-2013, 2013.

Morrison, H., and Gettelman, A.: A new two-moment bulk stratiform cloud microphysics scheme in the Community Atmosphere Model, version 3 (CAM3). Part I: Description and numerical tests, J. Climate, 21, 3642-3659, https://doi.org/10.1175/2008JCLI2105.1, 2008.

Neale, R. B., Richter, J. H., and Jochum, M.: The impact of convection on ENSO: from a delayed oscillator to a series of events, J. Climate, 21, 5904-5924, https://doi.org/10.1175/2008JCLI2244.1, 2008.

Neale, R. B., Gettelman, A., Park, S., Chen, C.-C., Lauritzen, P. H., Williamson, D. L., Conley, A., J., Kinnison, D., Marsh, D., Smith, A. K., Lamarque, J.-F., Tilmes, S., Morrison, H., Cameron-Smith, P., Collins, W. D., Iacono, M. J., Liu, X., Rasch, P. J., and Taylor, M. A.: Description of the NCAR Community Atmosphere Model (CAM 5.0). NCAR Tech. Note, TN-486, 274 pp, National Center

659 for Atmospheric Research, Boulder, CO, USA, 2010.
660 Oleson, K. W., Lawrence, D. M., Bonan, G. B., Flanner, M. G., Kluzek, E., Lawrence, P. J., Levis, S.,
661 Swenson, S., C., Thornton, P. E., Dai, A., Decker, M., Dickinson, R., Feddema, J., Heald, C. L.,
662 Hoffman, F., Lamarque, J.-F., Mahowald, N., Niu, G.-Y., Qian, T., Randerson, J, Running, S.,
663 Sakaguchi, K, and Slater, A.: Technical description of version 4.0 of the Community Land Model
664 (CLM), Tech. Rep. NCAR/TN-478+STR, 257 pp, National Center for Atmospheric Research,
665 Boulder, CO, USA, 2010.
666 Pan, H., and Wu, W.: Implementing a mass flux convection parameterization package for the NMC
667 medium-range forecast model, Tech. Rep., NMC Office Note, No. 409, Washington D. C., 1995.
668 Park, S., and Bretherton, C. S.: The University of Washington shallow convection and moist turbulence
669 schemes and their impact on climate simulations with the Community Atmosphere Model, J.
670 Climate, 22(12), 3449-3469, https://doi.org/10.1175/2008JCLI2557.1, 2009.
671 Park, S., Bretherton, C. S., and Rasch, P. J.: Integrating cloud processes in the community atmosphere
672 model, version 5, Journal of Climate, 27, 6821–6856, 2014.
673 Peng, G., Meier, W. N., Scott, D., and Savoie, M.: A long-term and reproducible passive microwave
674 sea ice concentration data record for climate studies and monitoring, Earth Syst. Sci. Data, 5, 311-
675 318, https://doi.org/10.5194/essd-5-311-2013, 2013.
676 Pincus, R., Barker, H. W., and Morcrette, J.-J.: A fast, flexible, approximation technique for computing
677 radiative transfer in inhomogeneous cloud fields, J. Geophys. Res., 108, 4376,
678 https://doi.org/10.1029/2002JD003322, 2003.
679 Potter, G. L., Carriere, L., Hertz, J., Bosilovich, M., Duffy, D., Lee, T., and Williams, D. N.: Enabling
680 reanalysis research using the Collaborative Reanalysis Technical Environment (CREATE), B. Am.
681 Meteorol. Soc., 99, 677-687, https://doi.org/10.1175/BAMS-D-17-0174.1, 2018.
682 Rayner, N. A., Parker, D. E., Horton, E. B., Folland, C. K., Alexander, L. V., Rowell, D. P., Kent, E.
683 C., Kaplan, A.: Global analyses of sea surface temperature, sea ice, and night marine air

684 temperature since the late nineteenth century, J. Geophys. Res., 108, 4407,
685 https://doi.org/10.1029/2002JD002670, 2003.
686 Rohde, R., Muller, R. A., Jacobsen, R., Muller, E., Perlmutter, S., Rosenfeld, A., Wurtele, J., Groom,
687 D., and Wickham, C.: A new estimate of the average Earth surface land temperature spanning
688 1753 to 2011, Geoinfor. Geostat.: An Overview, 1:1, https://doi.org/10.4172/2327-4581.1000101,
689 2013
690 Seigneur, C., Hudischewskyj, A. B., Seinfeld, J. H., Whitby, K. T. and Whitby, E. R.: Simulation of
691 Aerosol Dynamics: A Comparative Review of Mathematical Models. Systems Applications, Inc.,
692 San Rafael, CA, USA, 1986.
693 Shiu, C.-J., Wang, Y.-C., Hsu, H.-H., Chen, W.-T., Pan, H.-L., Sun, R., Chen, Y.-H., and Chen, C.-A.:
694 A macrophysics scheme for climate models based on a probability density function, Geosci.
695 Model Dev. Discuss., https://doi.org/10.5194/gmd-2020-144, in review, 2020.
696 Skamarock, W. C., Klemp, J. B., Dudhia, J., Gill, D. O., Barker, Duda, M. G., Huang, X.-Y., Wang,
697 W., and Powers, J. G.: A description of the advanced research WRF version 3, NCAR Tech. Note
698 475+STR, 125 pp., National Center for Atmospheric Research, Boulder, CO, USA, 2005.
699 Smith, R., Jones, P., Briegleb, B., Bryan, F., Danabasoglu, G., Dennis, J., Dukowicz, J., Eden, C., Fox-
700 Kemper, B., Gent, P., Hecht, M., Jayne, S., Jochum, M., Large, W., Lindsay, K., Maltrud, M.,
701 Norton, N., Peacock, S., Vertenstein, M., and Yeager, S.: The Parallel Ocean Program (POP)
702 reference manual, Los Alamos National Laboratory Tech. Rep. LAUR-10-01853, 140 pp., 2010.
703 Sundqvist, H., E. Berge, and J. E. Kristjansson: Condensation and cloud parameterization studies with
704 a mesoscale numerical weather prediction model, Mon. Wea. Rev., 117, 1641-1657, 1989.
705 Taylor, K. E., Stouffer, R. J., and Meehl, G. A.: An overview of CMIP5 and the experiment design. B.
706 Am. Meteorol. Soc., 93, 485-498, https://doi.org/10.1175/BAMS-D-11-00094.1, 2012.
707 Tompkins, A. M.: The parameterization of cloud cover, ECMWF Technical Memorandum: Moist
708 Processes Lecture Note Series, available at

https://www.ecmwf.int/sites/default/files/elibrary/2005/16958-parametrization-cloud-cover.pdf, 2005.

Tsai, I.-C., Chen, J.-P., Lin, Y.-C., Chou, C. C.-K., and Chen, W.-N.: Numerical investigation of the coagulation mixing between dust and hygroscopic aerosol particles and its impacts, J. Geophys. Res. Atmos., https://doi.org/10.1002/2014JD022899, 2015.

Tsuang, B.-J., Tu, C.-Y., Tsai, J.-L., Dracup, J. A., Arpe, K., and Meyers, T.: A more accurate scheme for calculating Earths skin temperature, Climate Dynamics, 32 (2-3), 251-272, 2009.

Tu, C.-Y., and Tsuang, B.-J.: Cool-skin simulation by a one-column ocean model, Geophys. Res. Letters, 32 (22), 2005.

Wang, C.-c., Lee, W.-L., Chen, Y.-L., and Hsu, H.-H.: Processes leading to double intertropical convergence zone bias in CESM1/CAM5, J. Climate, 28, 2900-2915, https://doi.org/10.1175/JCLI-D-14-00622.1, 2015a.

Wang, Y.-C., Pan, H.-L., and Hsu, H.-H.: Impacts of the triggering function of cumulus parameterization on warm-season diurnal rainfall cycles at the Atmospheric Radiation Measurement Southern Great Plains site, J. Geophys. Res. Atmos., 120, 10681-10702, https://doi.org/10.1002/2015JD023337, 2015b.

Wang, Y.-C., and Hsu, H.-H.: Improving diurnal rainfall phase over the Southern Great Plains in warm seasons by using a convective triggering design, International Journal of Climatology, 39, 5181-5190, https://doi.org/10.1002/joc.6117, 2019.

Whitby, E. R., and McMurry, P. H.: Model aerosol dynamics modeling, Aerosol Science and Technology, 27:6, 673-688, https://doi.org/10.1080/02786829708965504, 1997.

Xie, S., Wang, Y.-C., Lin, W., Ma, H.-Y., Tang, Q., Tang, S., Zheng, X., Golaz, J.-C., Zhang, G. J., and Zhang, M.: Improved diurnal cycle of precipitation in E3SM with a revised convective triggering function. Journal of Advances in Modeling Earth Systems, 11, 2290-2310, https://doi.org/10.1029/2019MS001702, 2019.

734 Zhang, G. J., and McFarlane, N. A.: Sensitivity of climate simulations to the parameterization of
735 cumulus convection in the Canadian Climate Centre general circulation model, Atmos.-Ocean,
736 33(3), 407-446, https://doi.org/10.1080/07055900.1995.9649539, 1995.
737

Variable	CESM1.2.2	TaiESM
SAT[a] (°C)	13.16	13.58
SST[b] (°C)	19.52	19.75
TOA net flux (W m^{-2})	0.080	0.089
TOA net SW flux (W m^{-2})	237.79	240.03
TOA net LW flux (W m^{-2})	237.71	239.94
TOA clear-sky net SW flux (W m^{-2})	285.41	286.07
TOA clear-sky net LW flux (W m^{-2})	260.35	262.02
SWCF (W m^{-2})	−47.62	−46.05
LWCF (W m^{-2})	22.67	22.08
High cloud cover (%)	37.81	45.61
Low cloud cover (%)	41.96	41.99

738 [a] Estimated observation value of SAT is 13.63°C from BEST (Rohde et al., 2013)

739 [b] Estimated observation value of SST is 19.27°C in 1854 from ERSST (Huang et al., 2017)

740

741 **Table 1.** Long-term global means of selected climatological variables from CESM1.2.2 and TaiESM

742

743 **Figure List**

744 **Figure 1.** Peak phase of diurnal rainfall cycle over three major tropical regions: Central Africa,
745 Southeast Asia, and Amazonia in (a) TRMM3B42 (2001–2011), (b) CESM1.2.2 (1979–2005), and
746 (c) TaiESM (1979–2005). Areas with amplitude of diurnal precipitation smaller than 0.5 mm day-
747 1 are masked out.

748 **Figure 2.** Time-longitude Hovmöller diagrams for diurnal rainfall cycle over the SGP observed by
749 TRMM3B42 dataset (2001–2011, upper panel), and simulated by CESM1.2.2 (central panel) and
750 TaiESM (lower panel), with the elevation of topography on the top.

751 **Figure 3.** Theoretical calculations of cloud fraction as a function of RH for water vapor and
752 condensates: (a) CAM5 macrophysics scheme, (b) GTS macrophysics with uniform PDF, and (c)
753 GRS macrophysics with triangular PDF.

754 **Figure 4.** A 500-year time series of annual mean climatological quantities in TaiESM piControl
755 simulation (from top to bottom): SAT at 2-m height, SST, net flux at the TOA (FNT), net flux at
756 the surface (FNS), SSS, volume-averaged ocean temperature, volume-averaged ocean salinity, and
757 NH and SH sea ice areas. The horizontal lines in FNT and FNS indicate the zero value.

758 **Figure 5.** Historical global mean SAT anomalies relative to the period of 1951–1980 from TaiESM
759 historical simulation (red) and observational datasets of BEST (blue) and GISTEMP (black).

760 **Figure 6.** Vertically integrated cloud fractions for (a) total cloud, (b) high cloud, and (c) low cloud in
761 the 1979–2005 TaiESM historical run (top panels), observations (MODIS for total cloud and
762 CloudSat–CALIOP for high and low cloud, central panels) and biases (bottom panels).

763 **Figure 7.** Cloud forcing for (a) shortwave and (b) longwave in the 1979–2005 TaiESM historical run
764 (top panels), observations (central panels, CERES–EBAF), and biases (bottom panels).

765 **Figure 8.** (a) SST and (b) SAT in the 1979–2005 TaiESM historical run (top panels), observations
766 (HadISST for SST and BEST for SAT, central panels), and biases (bottom panels).

767 **Figure 9.** Precipitation in the 1979–2005 TaiESM historical run (top panels), observations (GPCP,

768 central panels), and biases (bottom panels).

769 **Figure 10.** Annual mean sea ice concentration in the 1979–2005 TaiESM historical run for both NH
770 and SH. The solid black lines indicate the 15% sea ice concentration from the observation (NSIDC–
771 CDR, 1979–2005).

772 **Figure 11.** Time series of annual mean total sea ice area for both NH and SH from TaiESM historical
773 run and observation.

774 **Figure 12.** Power spectra of Nino 3.4 index from TaiESM (thin black line) and HadISST (thick gray
775 line) during 1976-2005. Color curves indicate the levels of significance at 99% (green), 95% (blue),
776 and 90% (red).

777 **Figure 13.** Composite anomalies of surface temperature (shading), sea level pressure (contour), and
778 near-surface wind (arrow) in December-February during El-Niño years. There are six and five El-
779 Niño events during 1976-2005 in TaiESM simulation (top panel) and Observation (bottom panel),
780 respectively.

781 **Figure 14.** The space-time RMSEs of upward longwave radiation at TOA in total sky and clear sky
782 (RLUT and RLUTCS), upward shortwave radiation at TOA in total sky and clear sky (RSUT and
783 RSUTCS), precipitation (PR), surface air temperature (TAS), geopotential height (ZG), meridional
784 wind (VA), zonal wind (UA), and air temperature (TA) from TaiESM, CMIP5 models, and CMIP5
785 MME. The values of shading represent the magnitude of normalized error with respect to the
786 median CMIP5 error. For example, a value of -0.2 indicates that the RMSE of a model is 20%
787 smaller than the median error.

788

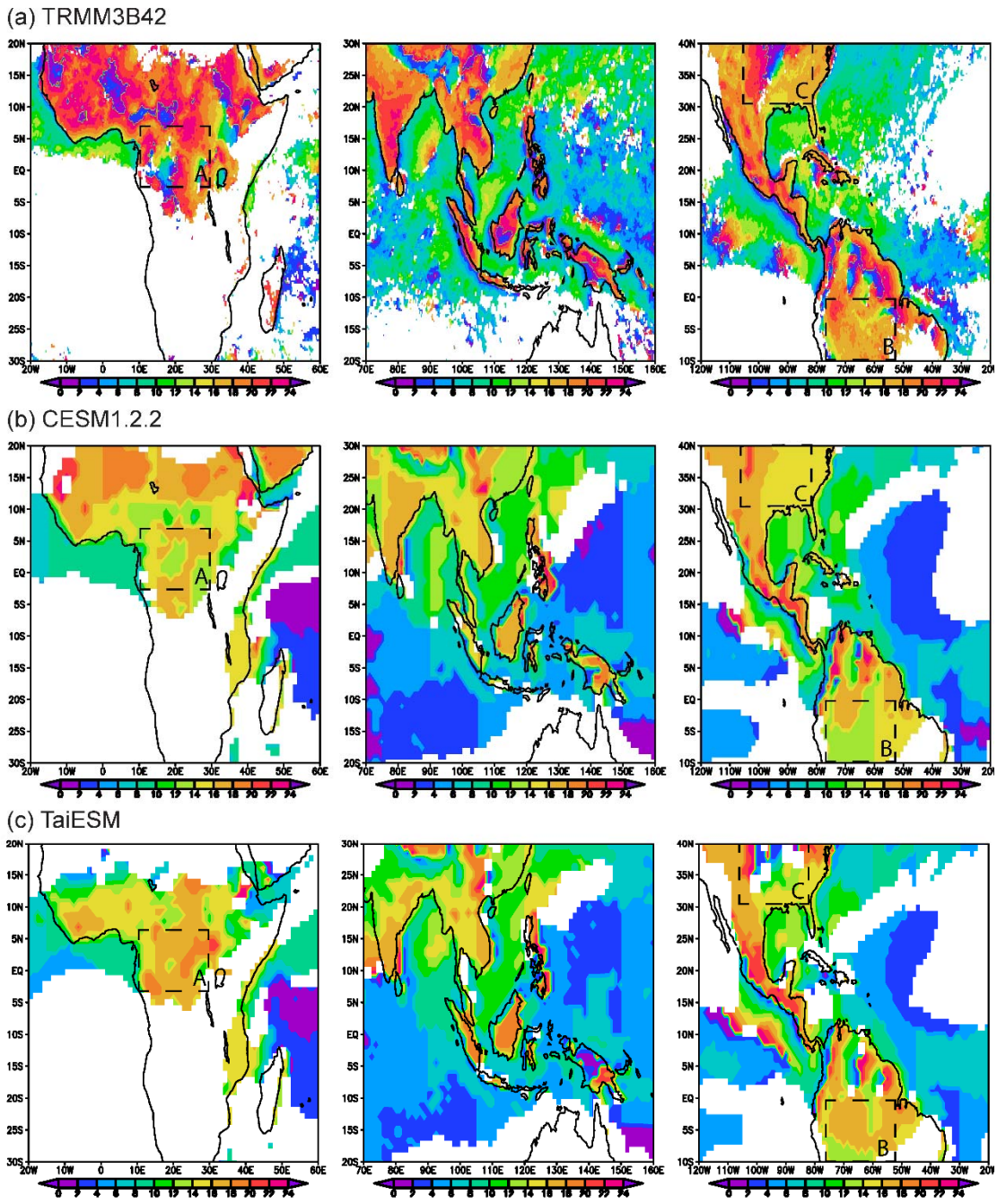

789

790 **Figure 1.** Peak phase of diurnal rainfall cycle over three major tropical regions: central Africa,
791 Southeast Asia, and Amazonia in (a) TRMM3B42 (2001–2011), (b) CESM1.2.2 (1979–2005), and (c)
792 TaiESM (1979–2005). Areas with amplitude of diurnal precipitation smaller than 0.5 mm day-1 are
793 masked out.

794

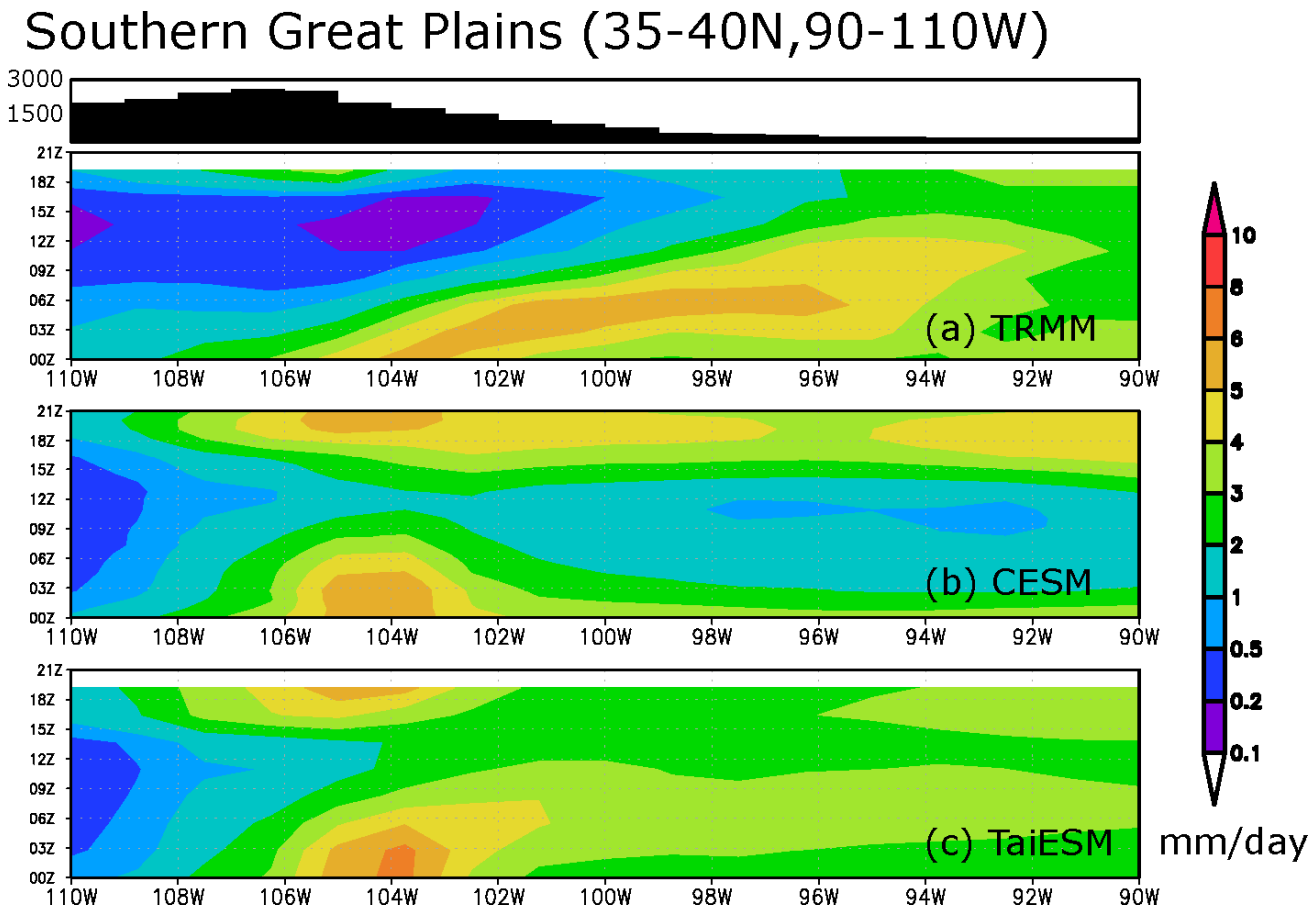

Figure 2. Time-longitude Hovmöller diagrams for diurnal rainfall cycle over the SGP observed by TRMM3B42 dataset (2001–2011, upper panel), and simulated by CESM1.2.2 (central panel) and TaiESM (lower panel), with the elevation of topography on the top.

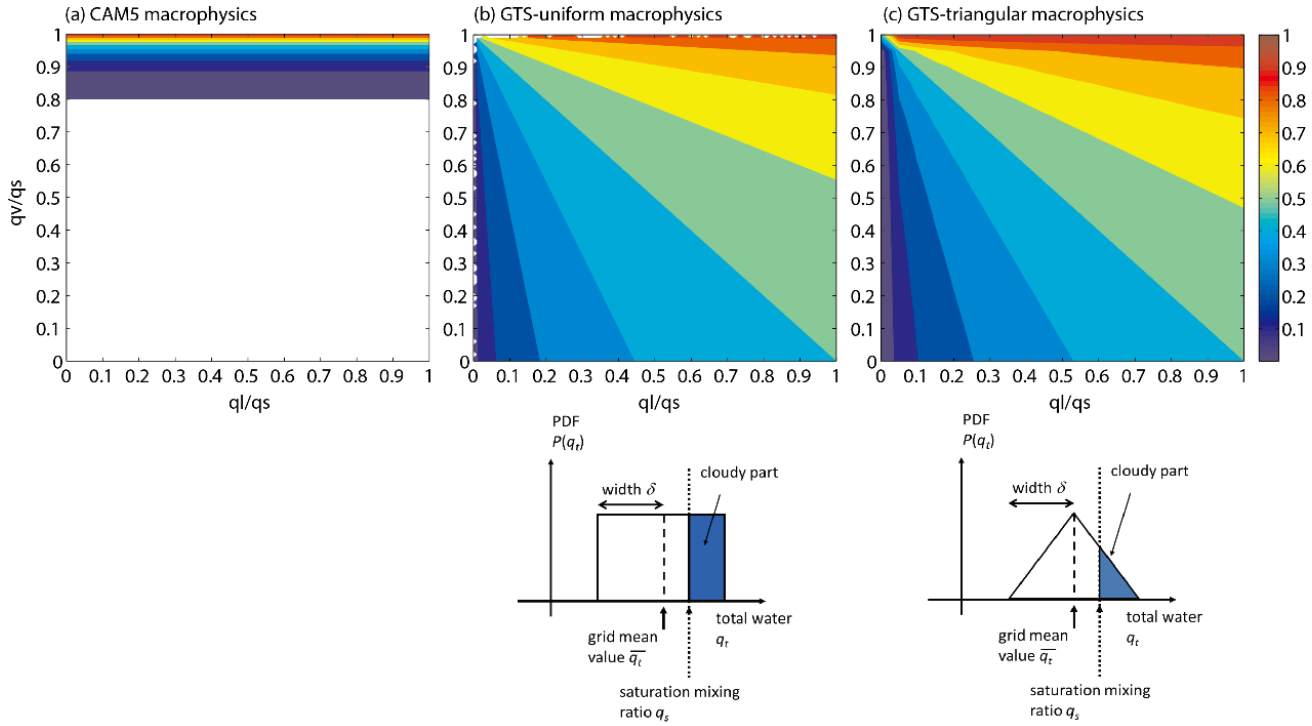

801

802 **Figure 3.** Theoretical calculations of cloud fraction as a function of RH for water vapor and

803 condensates: (a) CAM5 macrophysics scheme, (b) GTS macrophysics with uniform PDF, and (c) GRS

804 macrophysics with triangular PDF.

805

806

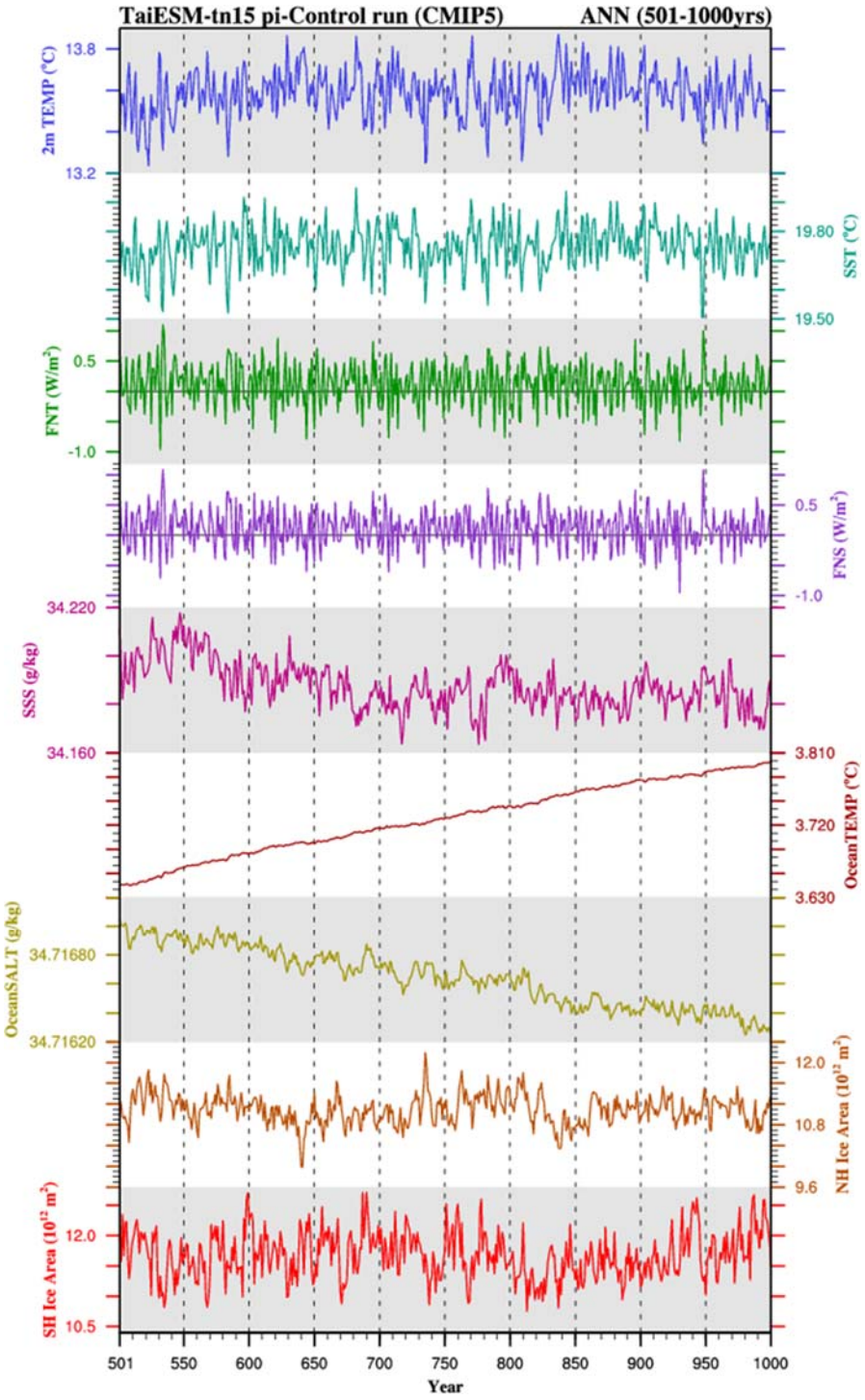

807

808 **Figure 4.** A 500-year time series of annual mean climatological quantities in TaiESM piControl
809 simulation (from top to bottom): SAT at 2-m height, SST, net flux at the TOA (FNT), net flux at the
810 surface (FNS), SSS, volume-averaged ocean temperature, volume-averaged ocean salinity, and NH
811 and SH sea ice area. The horizontal lines in FNT and FNS indicate the zero value.

812

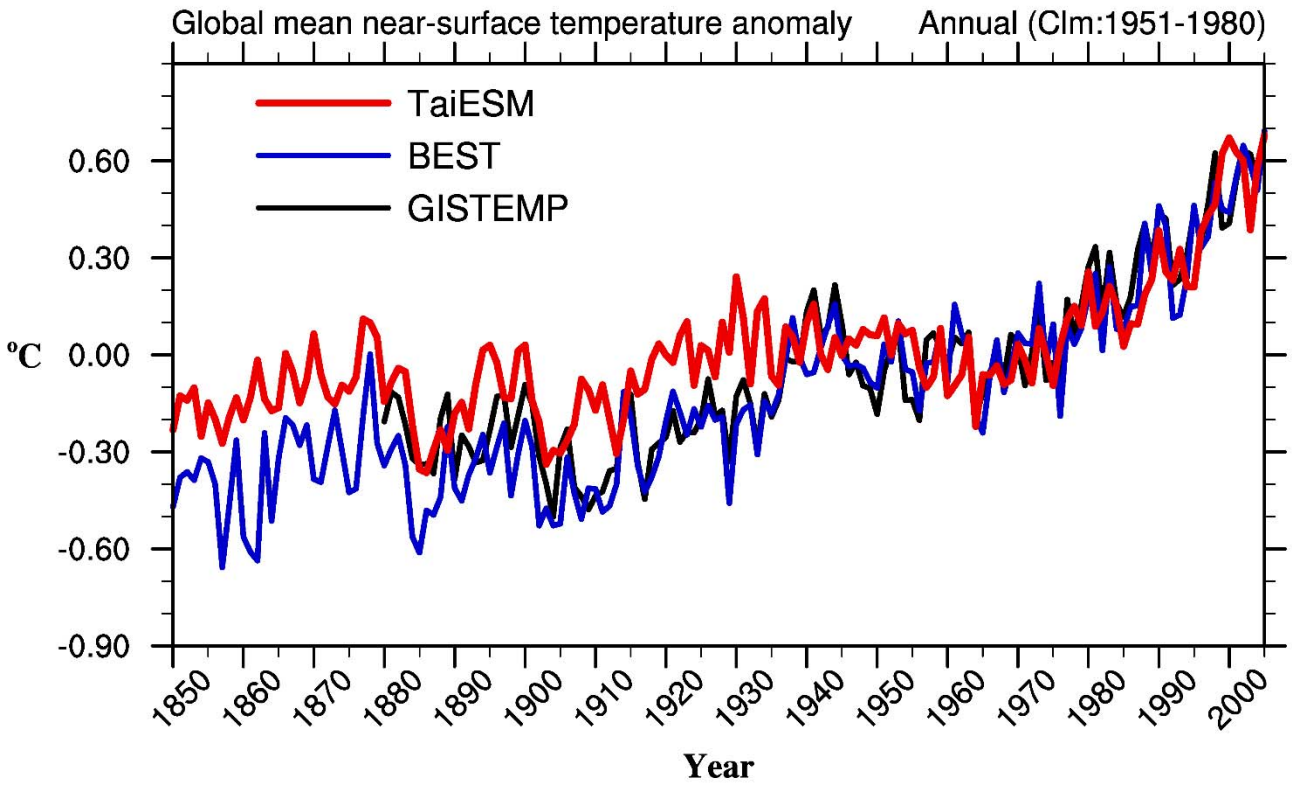

Figure 5. Historical global mean SAT anomalies relative to the period of 1951–1980 from TaiESM historical simulation (red) and observational datasets of BEST (blue) and GISTEMP (black).

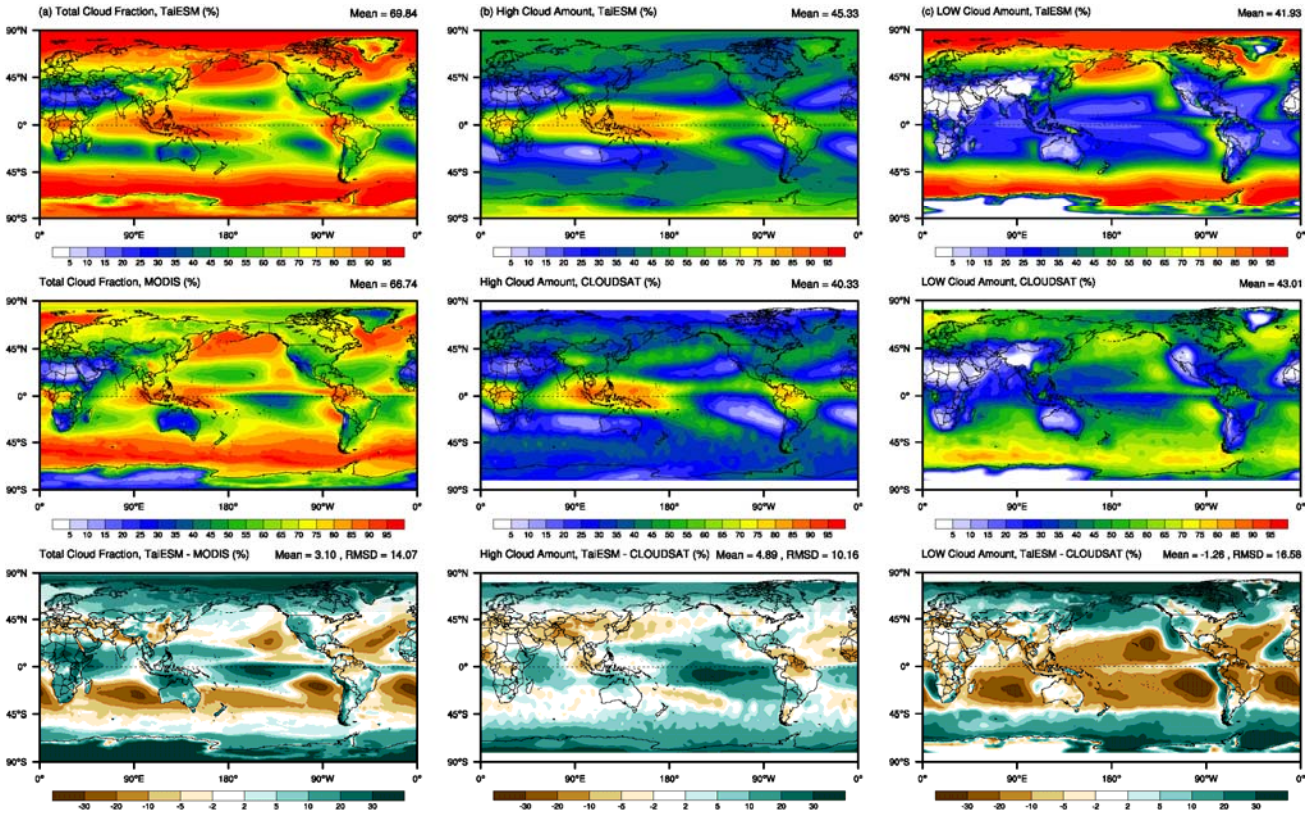

Figure 6. Vertically integrated cloud fractions for (a) total cloud, (b) high cloud, and (c) low cloud in the 1979–2005 TaiESM historical run (top panels), observations (MODIS for total cloud and CloudSat–CALIOP for high and low cloud, central panels) and biases (bottom panels).

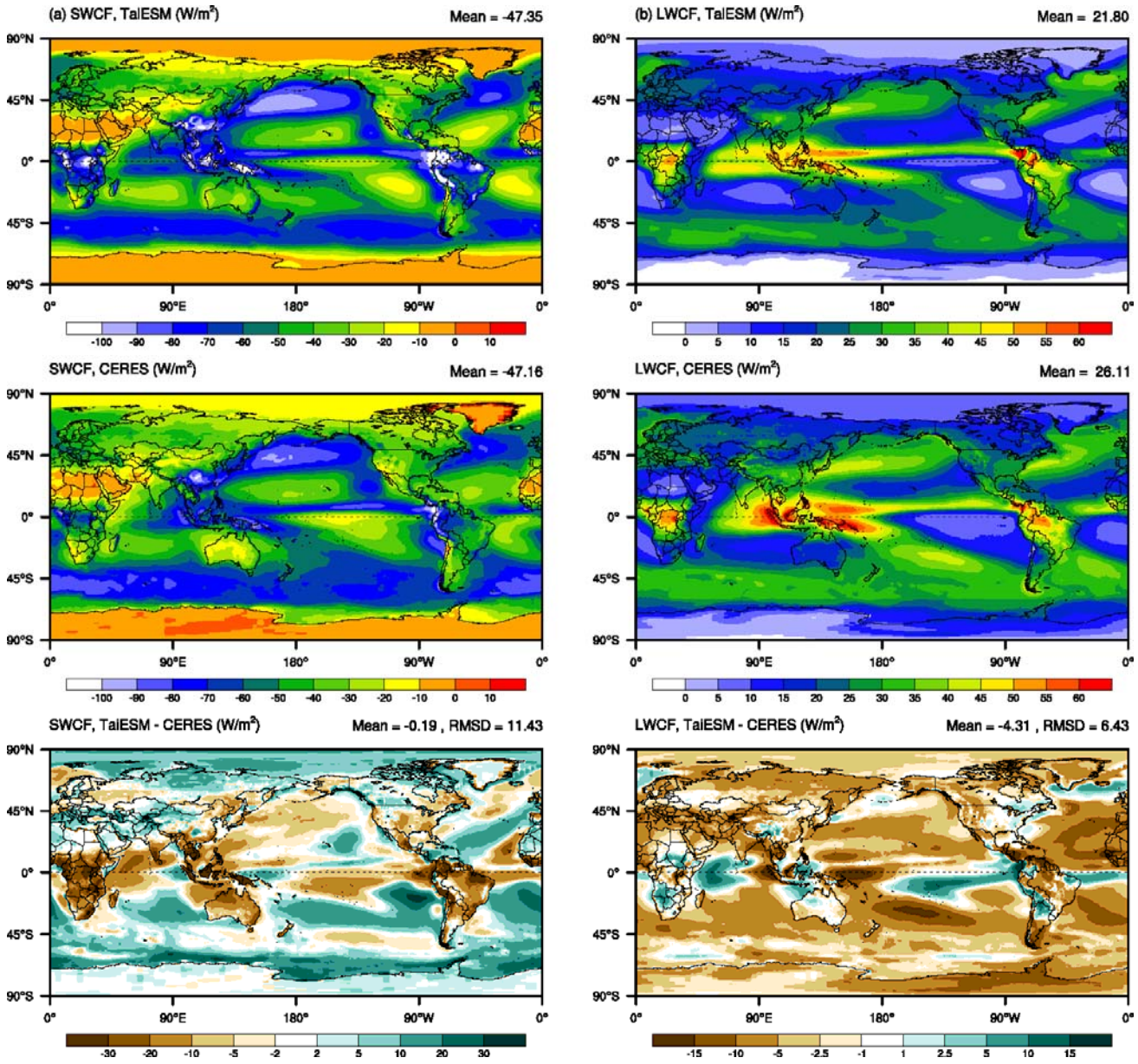

Figure 7. Cloud forcing for (a) shortwave and (b) longwave in the 1979–2005 TaiESM historical run (top panels), observations (central panels, CERES–EBAF), and biases (bottom panels).

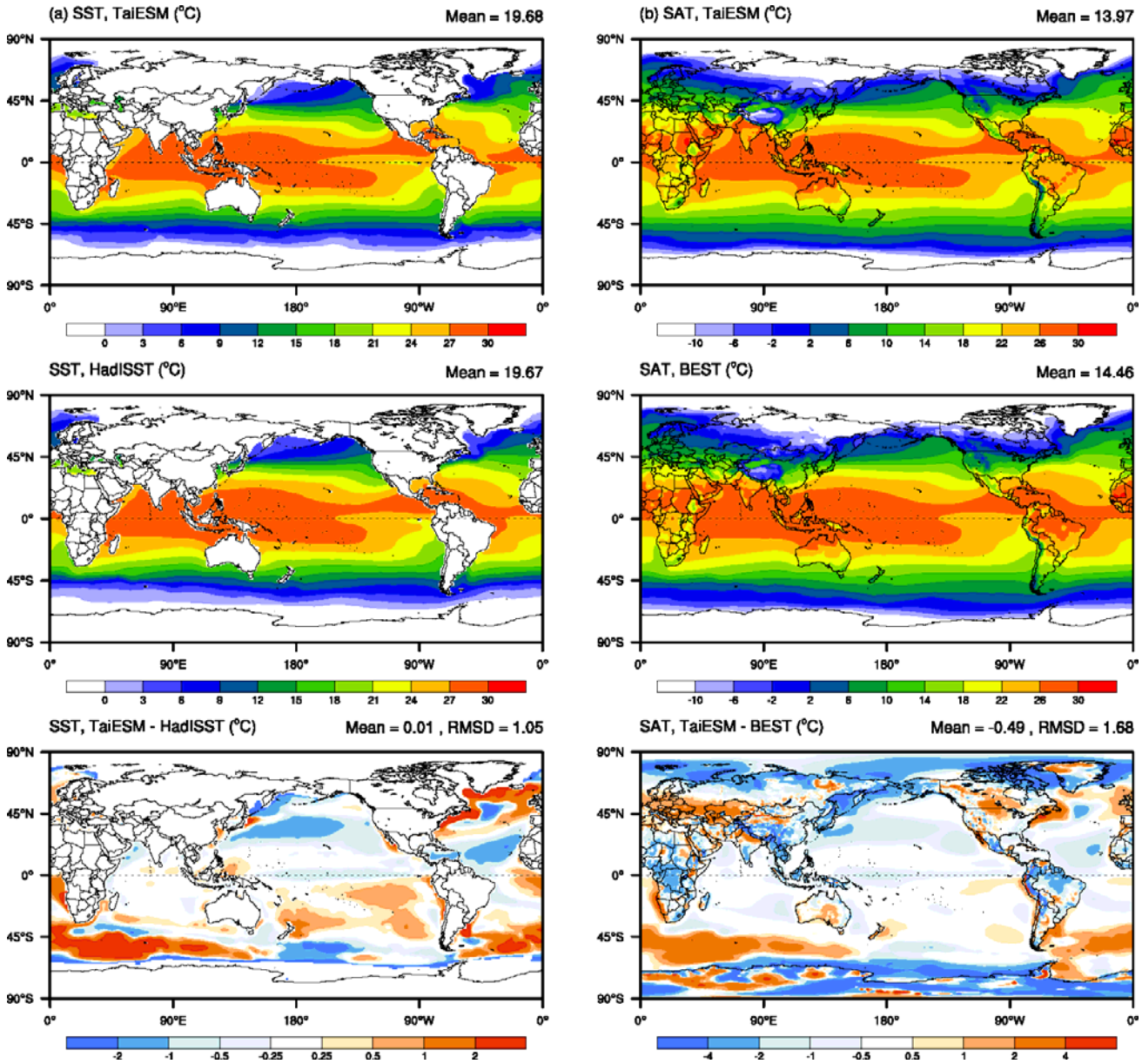

827

828 **Figure 8.** (a) SST and (b) SAT in the 1979–2005 TaiESM historical run (top panels), observations

829 (HadISST for SST and BEST for SAT, central panels), and biases (bottom panels).

830

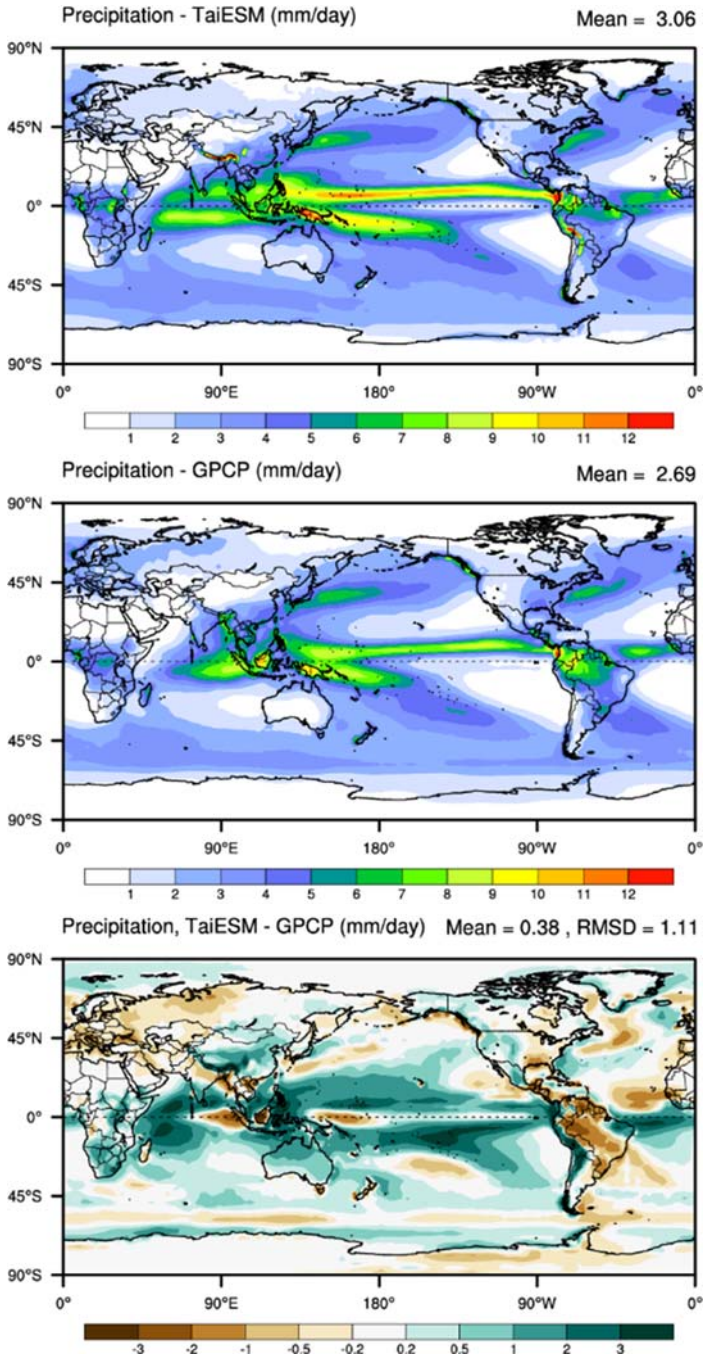

831

832 **Figure 9.** Precipitation in the 1979–2005 TaiESM historical run (top panels), observations (GPCP,

833 central panels), and biases (bottom panels).

834

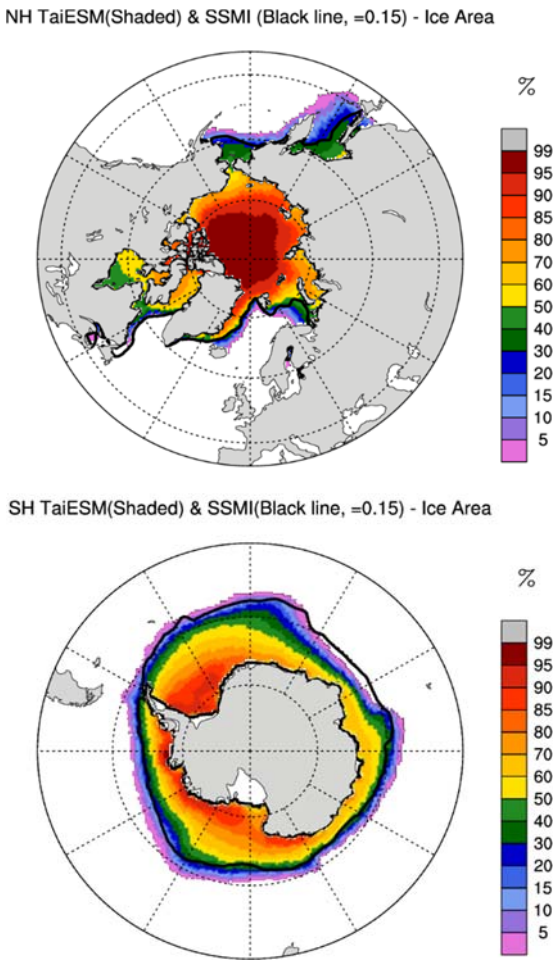

Figure 10. Annual mean sea ice concentration in the 1979–2005 TaiESM historical run for both NH and SH. The solid black lines indicate the 15% sea ice concentration from the observation (NSIDC–CDR, 1979–2005).

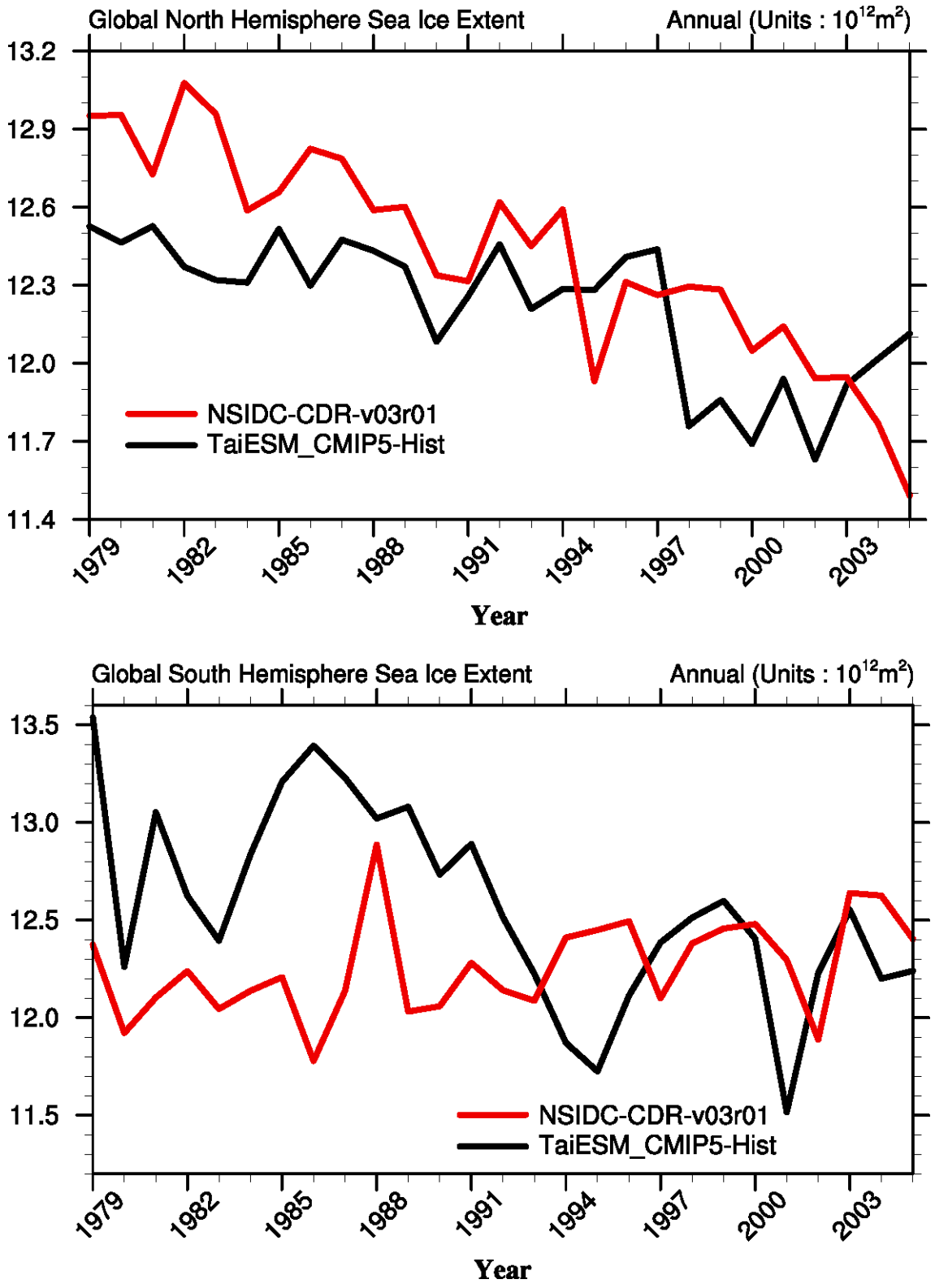

855

856 **Figure 11.** Time series of annual mean total sea ice area for both NH and SH from TaiESM historical

857 run and observation.

858

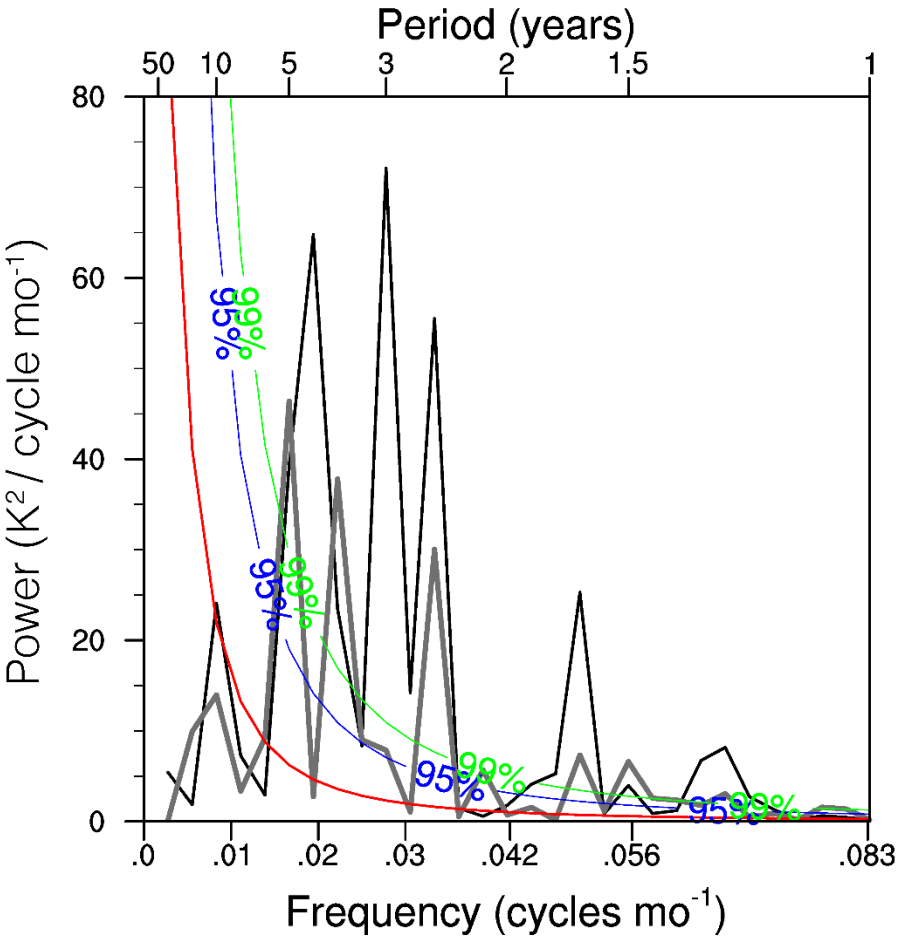

859

860 **Figure 12.** Power spectra of Nino 3.4 index from TaiESM (thin black line) and HadISST (thick gray

861 line) during 1976-2005. Color curves indicate the levels of significance at 99% (green), 95% (blue),

862 and 90% (red).

863

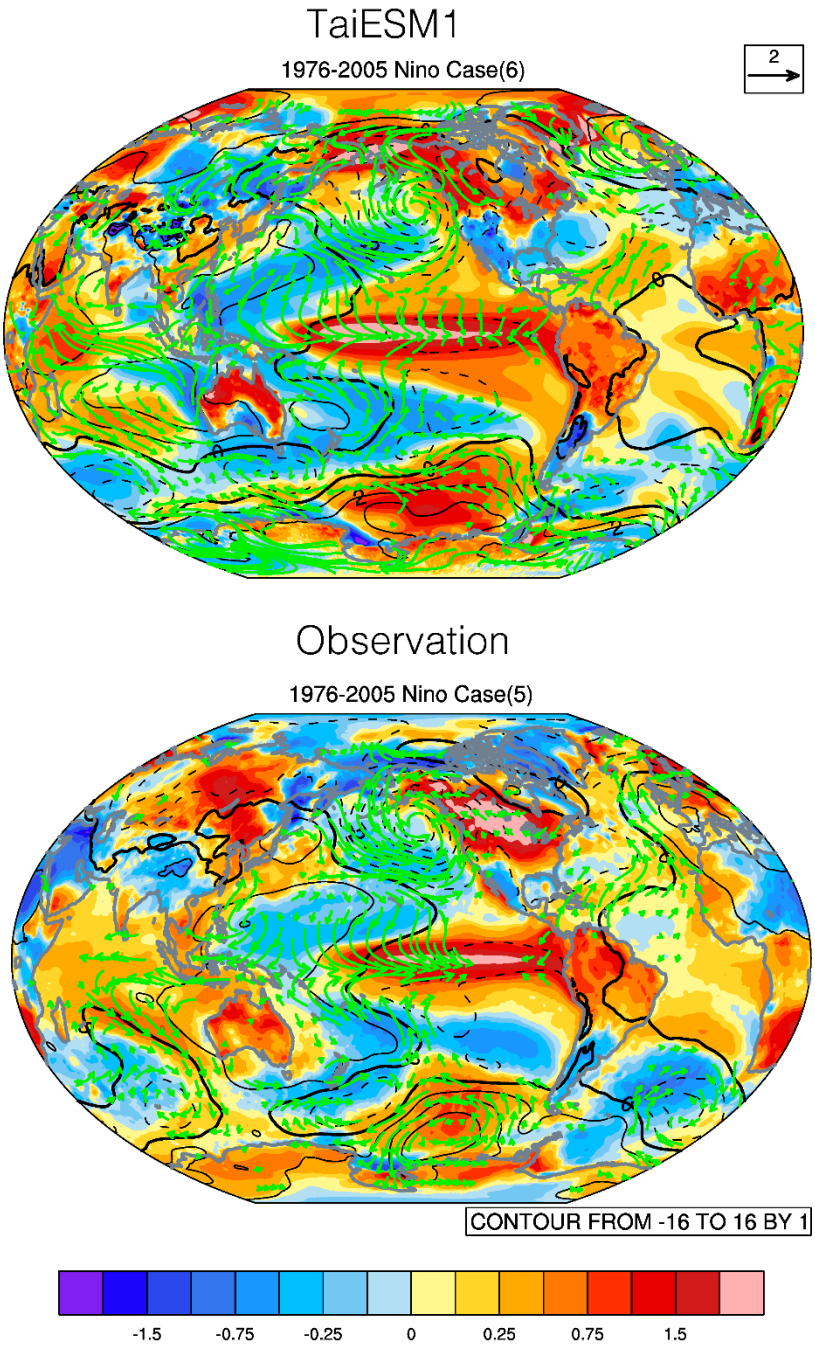

Figure 13. Composite anomalies of surface temperature (shading), sea level pressure (contour), and near-surface wind (arrow) in December-February during El-Niño years. There are six and five El-Niño events during 1976-2005 in TaiESM simulation (top panel) and Observation (bottom panel), respectively.

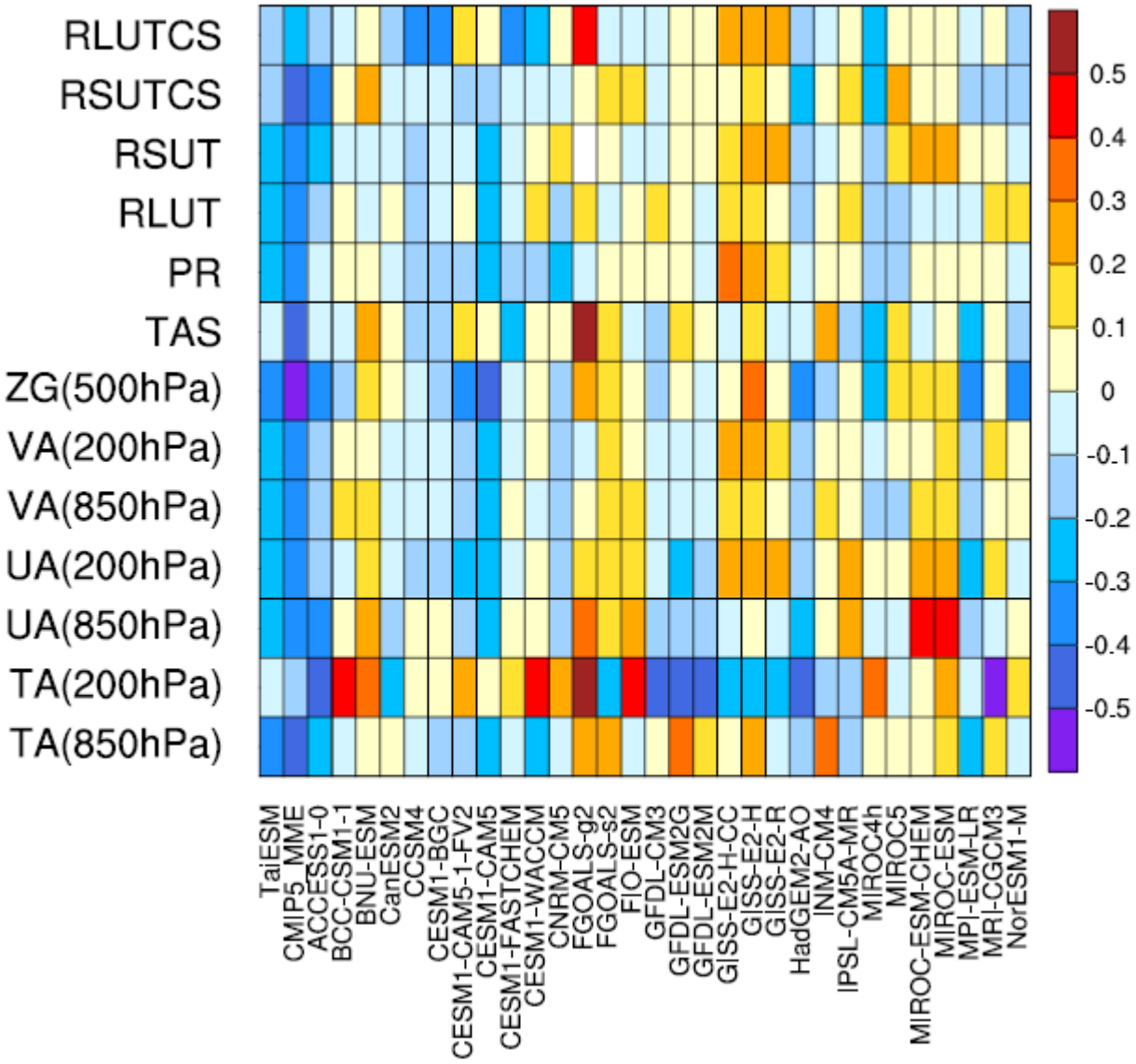

Figure 14. The space-time RMSEs of upward longwave radiation at TOA in total sky and clear sky (RLUT and RLUTCS), upward shortwave radiation at TOA in total sky and clear sky (RSUT and RSUTCS), precipitation (PR), surface air temperature (TAS), geopotential height (ZG), meridional wind (VA), zonal wind (UA), and air temperature (TA) from TaiESM, CMIP5 models, and CMIP5 MME. The values of shading represent the magnitude of normalized error with respect to the median CMIP5 error. For example, a value of -0.2 indicates that the RMSE of a model is 20% smaller than the median error.